UNIVERSITÀ DEGLI STUDI DI PARMA

Dottorato di Ricerca in Tecnologie dell'Informazione

XXIV Ciclo

Sensors for food industry: two cases of study

Coordinatore:

Chiar.mo Prof. Marco Locatelli

Tutor:

Chiar.mo Prof. Giovanni Chiorboli

Dottorando: *Cristian Tagliaferri*

Gennaio 2012

to my parents
that always support me
and always make me feel free

Contents

List of Figures

List of Tables

Preface

This work is intended as an overview of the main activities carried out during the 3-year doctorate course. Only the more relevant results, and the faced issues, will be reported in order to explain the logical path that motivated the design choices.

The research has concerned liquids analysis for food industry through two main techniques: impedance spectroscopy and ultrasounds. The first one has been the primary subject for the first part of the course, while the latter has been developed in the last year. In addition, during these years, a pulsed flow monitoring system (not for the food industry) has been designed as a fringe activity.

Impedance spectroscopy has been applied to the quality control for the dairy industry in order to support classical laboratory analyses by continuous, in-line, measurements. Direct reports, from the production chain, of possible abnormalities in the electrical parameters will increase the efficiency of the system and the quality of the final product. In particular, the sensitivity to some milk adulterants of not functionalized InterDigitated Array Microelectrodes sensors, IDAMs, has been analysed.

Functionalized IDAMs have been successfully used in recent years for detecting pathogenic bacteria, or contaminants, since they are able to emphasize the contribution of materials on their surface. If not functionalized IDAMs could detect other common adulterants, like water; an array of similar sensors (functionalized or not) might be used for a more complete characterization of beverages.

Initially, the effect of the sensor's geometry on the electric field has been investigated for understanding the thickness of the sensitive layer over the electrodes; then several measurements of different solutions (milk and water, milk and ammonia, etc.) in different environmental conditions have been performed.

Since a limiting condition for the IDAMs use was found in the measurements of high conductive solutions, a variable electrochemical cell, based on the classical parallel electrode configuration, has been designed. The distinctive feature of this new sensor was the adjustable gap between the electrodes. Two different prototypes were realized because of some sealing problems of the first one. This cell has been able to overcome the limitation of the IDAMs at the cost of a more complex measurement procedure.

The second technique developed, employing an ultrasonic sensor, concerns the continuous in-line measurement of substances concentration or density since it allows improving some industrial processes, for instance the primary fermentation of wine or beer.

The system is a time-of-flight (TOF) meter, which measures the ultrasonic velocity in the liquid, because density depends on the propagation speed of such pressure waves.

The whole system has been designed to transmit a front wave and read the pulsed oscillation on the receiver. A new technique has been studied for estimating the TOF and the design of the full-digital receiver depends on the results of several simulations. The complete system, with the receiver and the transmitter, has been implemented and characterized in its singular components, even if experimental results of the complete system are not currently available.

Finally, the fringe activity concerns the design and the verification of a flow monitoring system which must verify the correct functioning of a glue dispenser used in an industrial production process. The monitored flow has a pulsed behaviour with period of the order of seconds, therefore standard techniques cannot be used to compensate the sensor characteristics. The uncompensated output, coming from an anemometer used in constant temperature configuration, has been filtered to obtain a signal that will be compared with a reference waveform by an external microcontroller. The main issue of such an approach is the long settling time because of the low frequency poles of the filter. To speed up the response, the adaptive filter is able to modify its behaviour when a new start condition is detected: it temporarily becomes a simple buffer, so that its output can quickly reach values close to the correct ones, before to restore the normal filtering. In the last part of the control system, an optional circuit has been designed in order to substitute the external microcontroller. Such part is made of a peak detector that, synchronized with the mechanical dispenser, saves the peak value of the anemometer output and compare it with a fixed threshold. This allows to verify the dispensing of a minimum defined quantity of glue and detect possible blocks.

CHAPTER 1

IDAMs Sensors

1.1 Impedance Spectroscopy

1.1.1 Introduction to IS

Impedance spectroscopy, IS, is a technique for gathering physicochemical information of a substance from its response to a small signal stimulus. Analysis is generally carried out in the frequency domain and numerical data obtained from measurements are *post-processed* in order to point out more information compared to the simple impedance evaluation.

Classical procedures consist in applying a low voltage signal, generally less than 1 V to avoid electrochemical reactions as will be later explained, and measuring the magnitude and the phase of the flowing current. Depending on the electrical properties of the tested material, very large ranges of values are possible so that it is commonly more useful to express the measured values in two different ways:

- **Impedance (Z)**, i.e. the ratio of the applied voltage over the measured current, for low impedance values.
- **Admittance (Y)**, i.e. the ratio of the measured current over the applied voltage (the inverse of impedance), for high impedance values.

Impedance and admittance, in turn, can be written as:

$$Z = R + jX\,, \tag{1.1}$$

$$Y = G + jB\,, \tag{1.2}$$

where the **resistance**, R, and the **conductance**, G, are the real parts while the **reactance**, X, and the **susceptance**, B, are the imaginary parts of the impedance and the admittance, respectively.

When an insulator, or a high impedance material, is measured, another numerical representation is normally used by means of the **permittivity** (ϵ):

$$Y = j\omega\epsilon_r C_{vacuum} = j\omega\epsilon_r^{'} C_{vacuum} + \omega\epsilon_r^{''} C_{vacuum}\,, \tag{1.3}$$

where $\epsilon_r = \epsilon_r^{'} - j\epsilon_r^{''}$ is the complex relative permittivity and C_{vacuum} is the capacitance of the sensor in vacuum. The product $\omega\epsilon_r^{''}\epsilon_0$, where ϵ_0 is the vacuum permittivity equal to 8.85×10^{-12} F/m, is better known as **conductivity** (σ). The use of a complex permittivity allows to enclose the real part of the admittance, the losses, in the expression.

In impedance spectroscopy very different kind of sensors can be used, so different geometries are possible. The main problem in these situations is to find a way to compare measurements results because different geometrical dimensions lead to different absolute values of impedance. For this reason it is helpful to introduce the **cell constant**, K in m^{-1}, that takes into account the physical dimension contribution only. Using this parameter, distinctive of each sensor, the measured resistance and capacitance become:

$$R_{meas} = \rho_{MUT} \cdot K\,, \tag{1.4}$$

$$C_{meas} = \frac{\epsilon_0 \epsilon_{r_{MUT}}}{K}\,, \tag{1.5}$$

where ρ_{MUT} and $\epsilon_{r_{MUT}}$ are the **resistivity** (the inverse of the conductivity σ) and the relative permittivity of the Material Under Test, MUT, respectively. From Eqs. 1.4 and 1.5 it is so possible to obtain the physical parameters of the material regardless of the geometry of the sensor.

1.1.2 Metal-Electrolyte interface

When a metallic conductor is dipped in an electrolyte, i.e. a solution in which molecules dissociate in ions, the metal atoms directly touched by the liquid

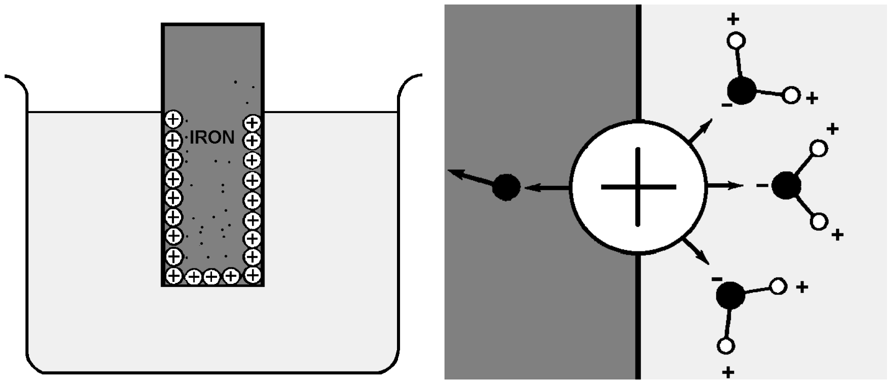

(a) *Adsorption of superficial metal ions.* (b) *Adsorption with polar liquids.*

Figure 1.1: Adsorption effect at the metal-electrolyte interface.

tend to ionize losing an electron. These electrons move inside the bar so that the bulk remains overall neutral.

The ionized metal atoms of the bar are electrostatically attracted to the metal surface but they cannot penetrate it as shown in Fig. 1.1(a). Such phenomenon is called the *adsorption* of the metal ions onto the surface of the object. The same effect is obtained using liquids made up of polar molecules in which atomic bonds make that different parts of the same molecule have different electrostatic charges. As an example, water molecules are polar because of their *banana-shape* and then it is possible to have the adsorbition effect (Fig. 1.1(b)).

The most important parameter for quantify such an effect is the reactivity of the metal: reactive metals ionize very easily because of their weak electrons attraction. Sodium and zinc atoms ionize easily oppositely to gold or platinum that hardly ionize.

Ionization depends on several forces that play different roles on the final balance:

- polar molecules encourage metal surface ionization;
- recombination in the metal reduces ions amount;
- negative voltage applied to the bar produces electrons excess that limits metal ionization;

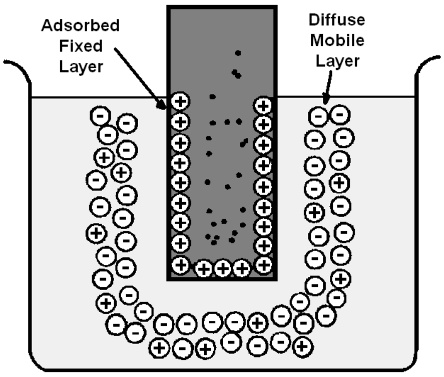

Figure 1.2: Double layer in a metal-electrolyte interface.

- positive voltage applied to the bar drains out electrons allowing new metal atoms to ionize.

Referring to Fig. 1.2, the metal ions adsorbed onto the plate form the **Adsorbed Fixed Layer** as well some negative charged ions in the electrolyte are attracted to the same metal ion layer forming a **Diffuse Mobile Layer**. These two layers together are called **Electrical Double Layer** and their behaviour is quite similar to the capacitor's one.

As above mentioned, applying a positive voltage to the metal plate, some electrons are drained out leaving some metal ions free to move into the electrolyte. The final result is that the neutral charge of the bar is restored. At this point other atoms are able to ionize according to the metal reactivity and so new free electrons are generated and ready to be drained out from the battery. Therefore this process allows a constant current flow (consuming the electrode) similar, in the electronic circuit theory, to a resistive behaviour . This resistance is named **Faradaic Resistance**.

Using an alternate voltage generator instead of the continuous voltage one, a different effect is obtained because no corrosion effects are involved when no net flow of current is present. The diffuse mobile layer, made up of negative ions, is placed to a short distance from the bar proportional to the charge of the free electrons, negative as well, in the metal. Removing free electrons reduces the electrostatic repulsion with negative ions in the electrolyte so the mobile layer is able to move closer to the metal surface. In an opposite way, adding electrons extend the influence area of the negative charge in the metal

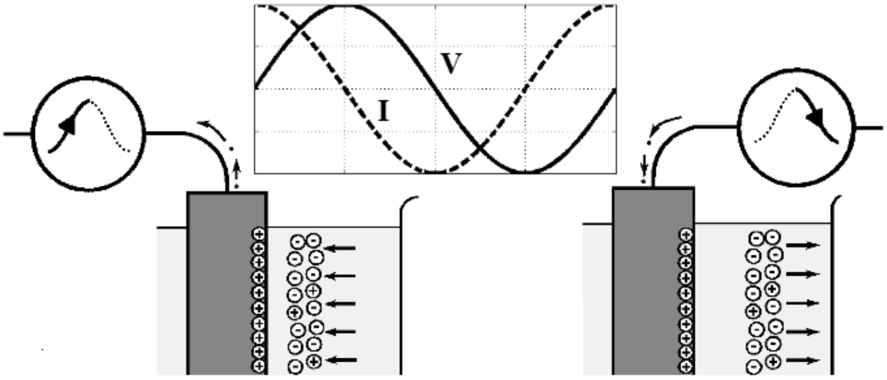

Figure 1.3: Capacitive behaviour of the *diffuse mobile layer* and the *adsorbed fixed layer* on the whole.

so the mobile layer is forced to move away from the plate. Adding or removing negative charge is equivalent to reduce or, respectively, increase the electric potential and, as illustrated in Fig. 1.3, current is 90° earlier than the potential showing a typical capacitive behaviour. Such a behaviour is modelled using the well known **Double Layer Capacitor**.

Actually the real situation at metal-electrolyte interface is more complex and less defined. In Fig. 1.4 are reported several layers that better describe the system:

- **Inner Helmholtz Plane (ihp)** referred to the metal ions adsorbed onto the metal electrode;

- **Outer Helmholtz Plane (ohp)** is the closest distance to the electrode for the free solvated electrolyte ions;

- **Diffuse Region of Charge** is the area in which electrolyte ions can still influence the interface behaviour. This region has a characteristic Debye length, which is typically on the order of 10 Å;

- **Diffusion Layer** is the last zone in which the interface affects the free ions in the electrolyte; the ions concentration quickly return to neutrality moving away in the bulk;

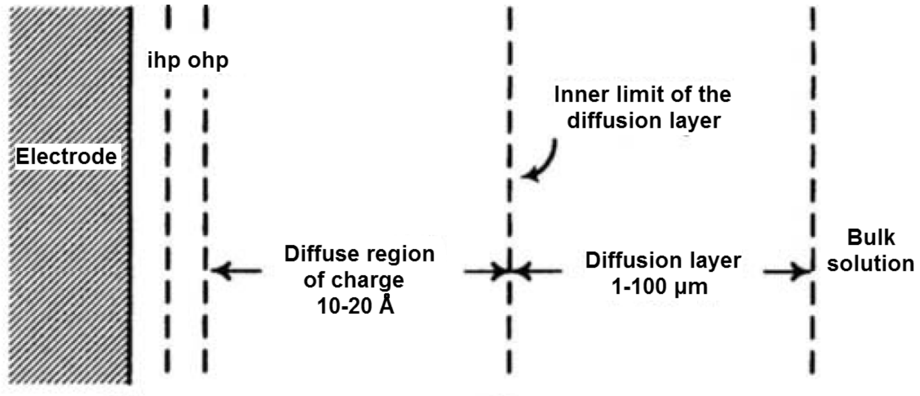

Figure 1.4: More realistic schematization of metal-electrolyte interface.

- **Bulk Solution** is not affected by influences and ions are randomly distributed.

Only the first three layers (ihp, ohp, and the diffuse region of charge) are considered to be part of the interface.

Having a closer look at the electrochemical system subjected to an external potential difference, it is possible to write:

$$V(I) = E + \eta + R \cdot I\,, \tag{1.6}$$

where V(I) is the potential applied to the electrodes (the metal plate and the electrolyte), E the internal potential in equilibrium state (without any external stimulus applied), R is the electrolyte resistance, I the current in the system and η is the *overvoltage* element that include every unbalanced phenomenon like the activation overvoltage and the concentration overvoltage (diffusion, reaction and crystallization).

The activation overvoltage is the potential used for the charge transfer (ionization and recombination) and it represents a typical threshold reaction so that only the atoms with higher energy than the activation threshold are able to react.

According to the polarity of the applied potential, two opposite reactions are possible:

- Anodic reaction $M \longrightarrow M^+ + e^-$ (oxidation)

- Cathodic reaction $M^+ + e^- \longrightarrow M$ (reduction)

which need an amount of energy equal to $W^{EQ}_{ATT,A}$ and $W^{EQ}_{ATT,C}$ in equilibrium state, respectively, and $W_{ATT,A}$ and $W_{ATT,C}$ in excited state. Fig. 1.5 shows the potential barrier in equilibrium and excited state; α is the symmetry factor of the barrier.

Paying attention that η is positive for anodic polarization and negative for cathodic polarization, from Fig. 1.5 it is easy to gather that:

$$W_{ATT,A} = W^{EQ}_{ATT,A} + zF\eta(1-\alpha) - zF\eta = W^{EQ}_{ATT,A} - \alpha zF\eta\,, \tag{1.7}$$

$$W_{ATT,C} = W^{EQ}_{ATT,C} + zF\eta(1-\alpha)\,, \tag{1.8}$$

where z is the number of free electrons generated in the ionization process and F is the Faraday Constant equal to 96 485 C/mol.

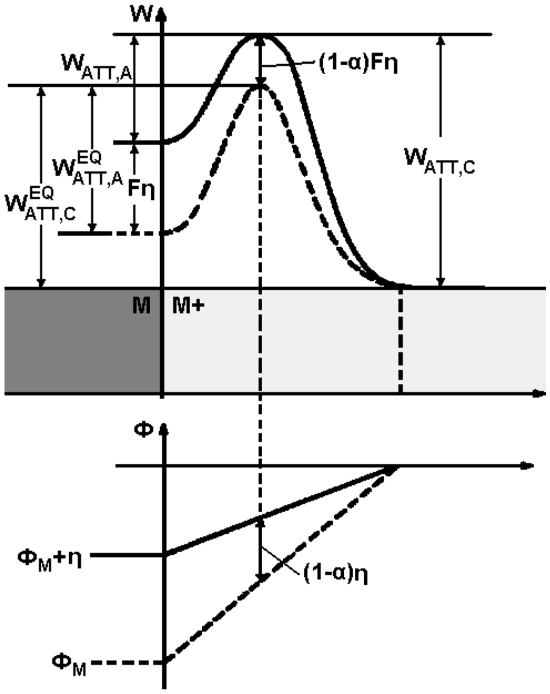

Figure 1.5: Energy and potential levels through the metal-electrolyte interface in equilibrium state (dashed line) and excited state (full line).

Using Arrhenius equation for the reaction rate, anodic and cathodic density currents can be written as:

$$j_A = zFk_A C_{red} e^{-\frac{W_{ATT,A}}{RT}} = zFk_A C_{red} e^{-\frac{W^{EQ}_{ATT,A} - \alpha zF\eta}{RT}} , \tag{1.9}$$

$$j_C = zFk_C C_{oxi} e^{-\frac{W_{ATT,C}}{RT}} = zFk_C C_{oxi} e^{-\frac{W^{EQ}_{ATT,C} + (1-\alpha)zF\eta}{RT}} , \tag{1.10}$$

where k is the kinetic constant of the reaction, C is the concentration of the reagents (reducing or oxidizing) and R is the ideal gas constant equal to 8.314 J/(K mol).

Without external excitation, at equilibrium ($\eta = 0$):

$$j_A = -j_C = j_0 = zFk_A C_{red} e^{-\frac{W^{EQ}_{ATT,A}}{RT}} . \tag{1.11}$$

Finally, adding both the contributions, the total current is:

$$j = j_A + j_C = j_0 (e^{\frac{\alpha zF\eta}{RT}} - e^{-\frac{(1-\alpha)zF\eta}{RT}}) . \tag{1.12}$$

Eq. 1.12 is known as the **Butler-Volmer equation** and is graphically reported in Fig. 1.6.

It is easy to notice that the electrical response of a metal-electrolyte interface is similar to an antiparallel diodes configuration's behaviour, so, in order to remain in quite linear conditions, signal amplitude used for the measurements has to be carefully chosen.

1.1.3 State of the art

The classical methods used in physiological analysis are based on chemical or biological techniques. These procedures take from several hours to some days so their in-line application is not possible and new ways have been sought.

Impedance measurements have been recently used for bacteria detection and quantification using special shaped sensors or bio-recognition elements on the surface of interdigitated electrodes [4, 5]. For example making up a planar microchannel so that cells are able to pass one by one, allows an accurate counting for low concentrations by measuring the impedance along the channel section. For higher concentrations, or growth monitoring, the interdigitated configuration is also used with success just reading the impedance of the bacteria layer that covers the fingers of the sensor [6, 7].

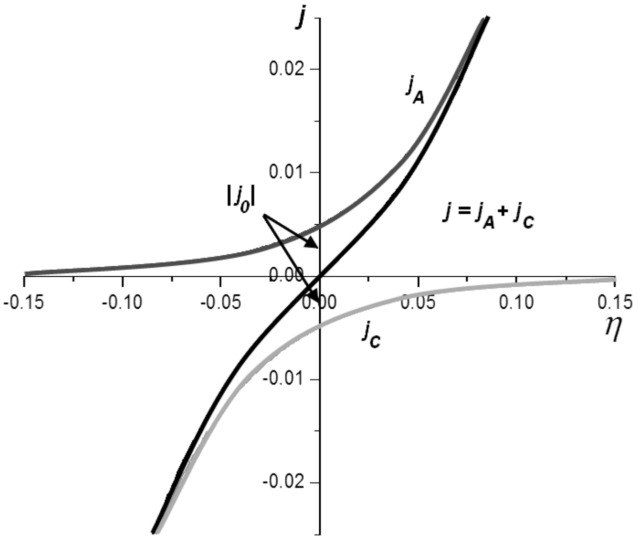

Figure 1.6: Butler-Voltmer equation for the current flowing through a metal-electrolyte interface.

Coupled with bio-recognition elements, which react with specific cells or molecule, the interdigitated electrodes are frequently used because of their high sensitivity close to their surface. When the target molecule reaches the selective material that cover the sensor, the bio-recognition element reacts changing its own impedance allowing an easy detection [4, 5, 8, 9, 10, 11]. With interdigitated sensors indirect measurements for cells growth control are also possible; instead of directly quantify the number of organisms, metabolites produced by bacterial cells, or even the charge of their internal components, can be monitored [5].

In dairy industry adulteration tests are a very common problem. Water addition slightly changes milk properties and this makes the detection hard. Cryogenic verification is the standard procedure because milk freezing point, normally occurred between −0.525 °C and −0.530 °C, depends on water percentage. The greater the amount of water, the higher the freezing point. The main problem in milk analysis is the variability of its composition, since season, breed cattle, cows diet and thermal processes can affect the freezing point. For that reason −0.520 °C is generally used as acceptable threshold.

Another remarkable problem is the addition of cooking salt to the milk used to mask the adulteration. As it is well known, salt is able to reduce the freezing point so the simultaneous addition of the correct water and salt combination can result in a freezing point similar to that of pure milk. Nowadays chloride analysis is used, together with cryogenic measurement, in order to check for adulteration of milk.

A further technique for determining the freezing point of milk is based on the Fourier transform infrared technology and some devices based on that principle are already commercially available [12].

Focusing on impedance measurements, their applicability in milk adulteration detection has already been verified using simple planar sensors [13, 14, 15, 16] or standard conductivity meters [17] showing a good sensitivity when ultra pure water is used. It is not clear the relation that connects the percentage of water with the conductivity of the milk because [15] reports a linear trend while [17] a power-law one. [16] also reports an unusual behaviour for 1-2 % of added water that suddenly reduces the conductivity of the milk to be later increased again for higher water concentrations.

Others conductivity measurements on the milk have been performed using commercial conductivity cells, or with couples of electrodes, to verify fat or cream content [18], synthetic milk [19], and acidification [20].

1.2 Sensor analysis

InterDigitated Array Microelectrodes, IDAMs, are planar sensors made of an insulating substrate on which a thin conductive layer is deposed and moulded to form an interdigitated configuration, see Fig. 1.7(a).

Impedance measurements with this kind of sensors are commonly used for specific bacteria detection covering the surface of the electrodes with biorecognition elements [4, 5, 8, 9, 10, 11]. These films are able to bind to themselves only the bacteria they are optimised for. As it will be better showed in the next sections, interdigitated sensors are able to analyse only a thin layer of solution next to their surface. The thickness of this layer directly depends on the gap between two sided fingers of the interdigitated sensor, so geometric parameters are crucial for each specific application: narrow gaps ensure no bulk influence whereas wide spaces allow thick solution layers to be involved. The greatest benefit of using these sensors in biological analysis is the remarkable time reduction, due to their ease of use, compared to the classical laboratory

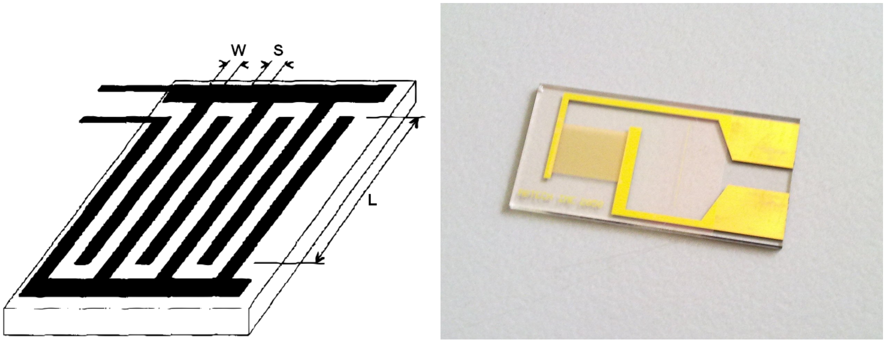

(a) *Interdigitated geometry.* (b) *Picture of the* ABTECH *sensor used.*

Figure 1.7: Interdigitated sensor.

methods that should be utilized for more detailed investigations anyway.

The same method can be exploited more times on the same substrate making a so called *Lab-on-a-Chip*, LOC, in which different interdigitated electrodes analyse the same solution at the same time but looking for different kinds of bacteria.

IDAMs are also used for bacteria counting and estimation when it is important to know the growing level in a culture [6, 7]. As above mentioned, the size of the fingers and the size of the bacteria influence the accuracy of the estimation.

This kind of sensor has been chosen, for our measurements, with the purpose of verifying its sensitivity in milk quality control and comparing the obtained results with other kind of sensors. The final target of this investigation is to explore the possibility of using IDAMs in the milk production and distribution chains, for a real *on-line* monitoring.

The IDAMs sensors used in the measurements are manufactured by the ABTECH SCIENTIFIC [21]. In Fig. 1.7(b) a picture of a **IME 2050.5 M-Au-U** sample is shown. Insulating substrate is made of 0.5 mm thick Schott D263 Borosilicate Glass (relative permittivity of 6.7 @ 1 MHz and resistivity of 1.6×10^8 Ω·cm) 2.00 cm long and 1.00 cm large. A 100 nm gold layer is deposed on the substrate and an interdigitated pattern is obtained using microlithographic techniques. Finally, a silicon nitride protection layer is placed on the sensor only leaving the interdigitated fingers and the bonding pads uncovered.

The sensing area, limited to the interdigitated fingers only, is composed of 50 couples of 4.980 mm long and 20 µm wide fingers. Interdigit spacing between fingers is 20 µm.

For a better understanding of the IDAM behaviour, two different approaches, analytical and numerical, have been followed. The first one allowed to quantify the electric field and the capacitance as a function of the interdigitated geometry whereas the second one, based on finite elements simulations, has been used as a comparison and check tool.

1.2.1 Analytical study

As already mentioned in the introduction, the key parameter of an impedance sensor is the cell constant which only depends on the geometrical dimensions. Through this value it is possible to find out the real electrical parameters of a solution, the conductivity σ and the permittivity ϵ, from a single measure.

In the technical datasheet of the IDAMs [22] a nominal value of $0.040\,\mathrm{cm}^{-1}$ for the cell constant K is reported, so that the theoretical capacitance in air should result:

$$\begin{aligned} C &= C_{air} + C_{glass} \\ &= \frac{\epsilon_0}{K} + \frac{\epsilon_0 \epsilon_{glass}}{K} \\ &= \frac{\epsilon_0}{K} \cdot (1 + \epsilon_{glass}) \\ &= \frac{8.85 \times 10^{-12}\,[\mathrm{F/m}]}{4\,[\mathrm{m}^{-1}]} \cdot (1 + 6.7) = 17.04\,\mathrm{pF}\,. \end{aligned} \tag{1.13}$$

As it is possible to notice in Eq. 1.13, the total capacitance is made of two contributions, one concerning the air over the interdigitated fingers and one ascribed to the glass of the substrate. In air, the resulting capacitance is mainly due to the substrate.

The cell constant can be determined by analysing the electric field around the sensor. In literature several analytical methods have been reported [23, 24, 25, 26, 27, 28], mostly based on the **conformal mapping technique**. Formally, a conformal map is a mathematical function which preserves angles. This transformation allows to map an harmonic function defined over a particular space, like an electromagnetic field, to another space preserving its harmonicity. In practical terms, it is possible to study the electric field of a complex geometry transforming it in a more convenient one.

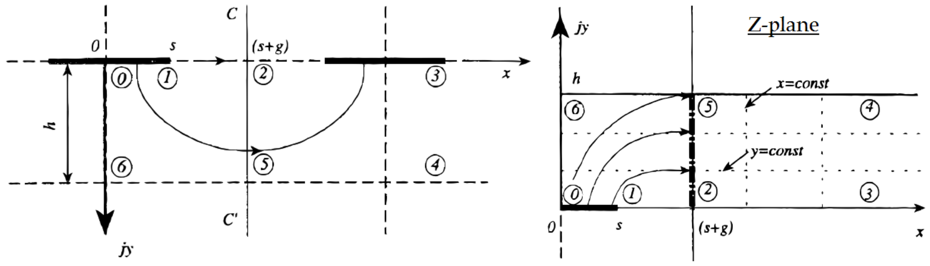

(a) *Original plane.* (b) *Transformation to Z-plane.*

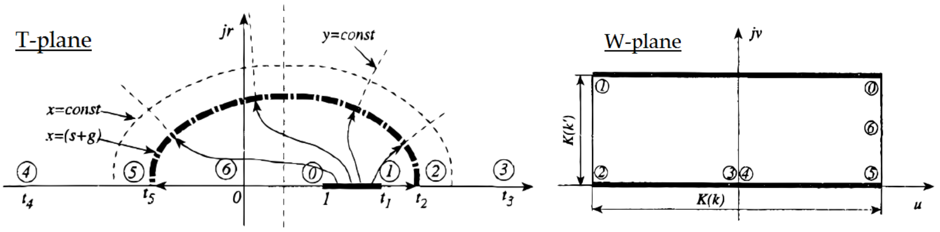

(c) *Transformation to T-plane.* (d) *Transformation to W-plane.*

Figure 1.8: Transformation of the section of a 2-finger interdigitated sensor using conformal mapping.

A deep literature study has been made with the aim of understanding this approach and allowing a more thorough comparison. Only a simplified review and a short discussion about the main distinctive features of several approaches will be reported.

Instead of considering the whole extension of an interdigitated sensor, it is more practical to reduce the analysis to two sided fingers only, so that the issue is limited to the analytical expression of the capacitance between two sided plates. In Fig. 1.8(a) the cross-section of the fingers is shown and only the beneath part will be considered in the estimation, the same equations will be applied to the over part for the symmetry of the geometry. That configuration can be further simplified, Fig. 1.8(b), using other symmetries: in a periodic system only the right half of a finger concurs to the capacitance with the finger on the right (similarly for the left half, with the left finger) and, furthermore, the system can be seen as the sum of a series of two capacitors of doubled value, using a virtual equipotential line along the CC' symmetry line.

At this point a Schwarz-Christoffel transformation is applied to map the 0346 polygon in the Z-plane to half plane of the T-plane using the mapping function:

$$t = \cosh^2\left(\frac{\pi z}{2h}\right). \tag{1.14}$$

As it is possible to see in Fig. 1.8(c), the whole perimeter of the 0346 polygon in the Z-plane is mapped onto the real axis of the T-plane and the vertices will assume new values:

$$\begin{aligned} &t_0 = 0\,, && t_1 = \cosh^2\left(\frac{\pi s}{2h}\right), && t_2 = \cosh^2\left(\frac{\pi(s+g)}{2h}\right), \\ &t_3 = t_4 = \infty\,, && t_5 = -\sinh^2\left(\frac{\pi(s+g)}{2h}\right), && t_6 = 0\,. \end{aligned}$$

Finally, the upper half of the T-plane is mapped onto the interior of a rectangle in another plane using again a Schwarz-Christoffel transformation:

$$\begin{aligned} w &= A\int_t^{t_5} \frac{dt}{(t-t_0)^{(1-\frac{\alpha}{\pi})}(t-t_1)^{(1-\frac{\beta}{\pi})}(t-t_2)^{(1-\frac{\gamma}{\pi})}(t-t_5)^{(1-\frac{\delta}{\pi})}} + B \\ &= A\int_t^{t_5} \frac{dt}{\sqrt{(t-t_0)(t-t_1)(t-t_2)(t-t_5)}} + B\,, \end{aligned} \tag{1.15}$$

where α, β, γ, δ are the angles of the vertices in the final W-plane, fixed to $\pi/2$ in a rectangle, and A and B are constants determined from the coordinates of the final rectangle, Fig. 1.8(d).

Only at this point, in the W-plane, it is possible to easily estimate the capacitance with the classical parallel plates equation. Afterwards, the result should be brought back to the original plane using the inverse functions of the mappings. As reported in [24] the final solution is:

$$C = \frac{1}{2}\epsilon_r\epsilon_0\frac{K(k)}{K(k')}\,, \tag{1.16}$$

where the 1/2 is due to the series of the two identical capacitance in which the system has been divided, $K(x)$ is the elliptic integral of the first kind, and k and k' are defined as:

$$k = \frac{\sinh\left(\frac{\pi s}{2h}\right)}{\sinh\left(\frac{\pi(s+g)}{2h}\right)} \cdot \sqrt{\frac{\cosh^2\left(\frac{\pi(s+g)}{2h}\right) + \sinh^2\left(\frac{\pi(s+g)}{2h}\right)}{\cosh^2\left(\frac{\pi s}{2h}\right) + \sinh^2\left(\frac{\pi(s+g)}{2h}\right)}}\,, \tag{1.17}$$

$$k' = \sqrt{1-k^2}\,. \tag{1.18}$$

The Eq. 1.16 is only valid for two central fingers of an interdigitated sensor with uniform dielectric; it includes the upper (or the lower) part only and its value should be intended per unit length. Therefore, this result should be multiplied for the pair of fingers of the sensor, for the fingers length and added to the other substrates or superstrates contributions.

From the total result it is easy to find out the cell constant:

$$K = \frac{\epsilon_0 \epsilon_r{}'}{C}\,, \tag{1.19}$$

where $\epsilon_r{}'$ is the composition of the permittivities of the several layers.

As just said, for a complete evaluation of a real sensor more detailed calculations must be done. A review of different methods is now reported:

1. **Olthuis** [23] uses a more elaborate transformation for mapping the whole two-finger configuration without simplification due to the symmetries. A simple multiplication for the number of gaps between the fingers is counted and a different expression for the two-finger configuration is provided.

2. **Gevorgian** [24] provides a very complete analysis of the interdigitated geometry taking into account:

    - the thickness of the fingers, increasing their effective width using Wheeler's first order approximation;
    - the different behaviour of the external fingers, on the basis of results obtained with a three-finger geometry;
    - multilayer substrate (or even superstrate) with different permittivity, by adding their individual contributions;
    - the capacitance due to the finger ends, obtained by applying again the conformal mapping;
    - the two or three-finger particular configurations.

3. **Igreja** [25] includes in the computation the different effect of the marginal fingers and the multilayer substrate or superstrate.

4. **Otter** [26] proposes a numerical approximation of the potential that allows reducing the computation to a sum of Bessel functions of the first kind; it refers only to two sided fingers of a larger array without others closer examinations.

Table 1.1: Analytical values of the constant cell for the ABTECH interdigitated sensor used in this work. Values with $\epsilon_r = 1$ over the sensor.

Method	Estimate
Nominal [22]	$4.000\,\mathrm{m}^{-1}$
Olthuis [23]	$4.057\,\mathrm{m}^{-1}$
Gevorgian [24]	$4.859\,\mathrm{m}^{-1}$
Igreja [25]	$4.039\,\mathrm{m}^{-1}$
Otter [26]	$4.014\,\mathrm{m}^{-1}$
Zaretsky [27]	$4.016\,\mathrm{m}^{-1}$

5. **Zaretsky** [27], starting from [28] and using fingers width equal to gaps width, shows that the cell constant is equal to $2/(NL)$ where N is the number of fingers and L their length. This analysis is not based on the conformal mapping but on a direct analysis of the electrical field distribution.

A table that summarize the numerical results of these methods (applied to the used sensor) is reported in Table 1.1. It can be noticed that, as reported in [25], the values computed with the Gevorgian model overestimate the constant K. The other models provide a good estimate, particularly those in [27] or in [26], if the correct number of electrodes is considered.

1.2.2 FEM simulations

Another technique to estimate the capacitance, and consequently the cell constant, is the numerical simulation with the finite element method. In this case the geometrical domain is divided in smaller parts on which the Maxwell equations will be solved and the solutions will be agreed with the corresponding ones calculated on the neighbouring subdomains.

Only a cross section of the sensor has been drawn for the simulation, so the resulting capacitance should be multiplied for the length of the facing fingers ($5\,\mathrm{mm}$ - $20\,\mu\mathrm{m}$ = $4.98\,\mathrm{mm}$) in order to achieve the overall value. The electric field lines are established in the glass substrate as well as in the air above the sensor, so it is necessary to draw these layers with a thickness that include most of the same field lines. As it is possible to see in Fig. 1.9, the electrical field intensity is reduced by half in the first $15\,\mu\mathrm{m}$ from the air/substrate interface

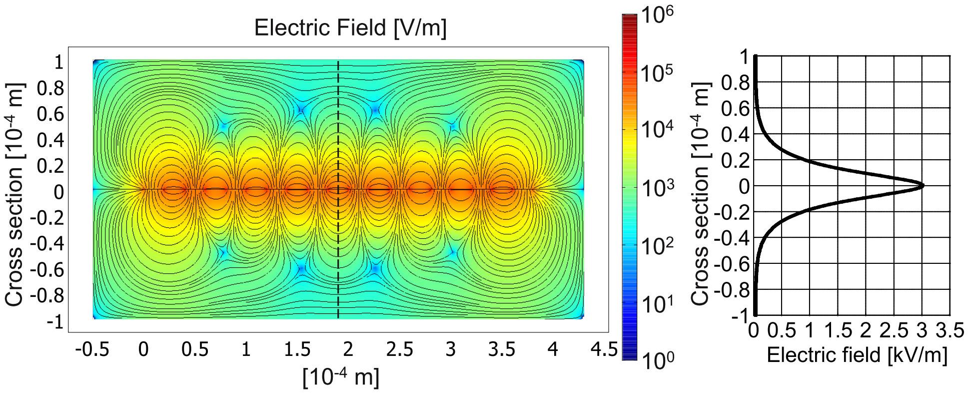

Figure 1.9: Cross-section view of electric field lines of a IDAM's FEM simulation (simplified geometry). Lower part is made of borosilicate glass while in the upper part $\epsilon_r = 1$ is imposed. It should be noticed that the electric field is not affected by different permittivity values. On the right, the electrical field intensity along the dashed line is shown.

and the main part is located in the first 100 µm. For this reason, 100 µm is the thickness used in the simulations.

As a boundary conditions, a potential of 1 V has been applied to the first finger on the right, grounding the second one and so on alternating the applied potential. The capacitance has been determined adding all the superficial charges built up on the fingers of the same branch and dividing them for the used differential potential (1 V).

A critical parameter for the results of the simulation is the amount of the mesh elements. Small quantities allow faster simulations but with limited accuracy, vice-versa higher numbers provide greater accuracy at the cost of long simulation times. In Tab. 1.2 the trend of the resulting capacitance for a whole 50-pair geometry is reported. It has been considered only the overhanging air for the simulation in order to reduce the complexity. For the mesh refinement, the adaptive algorithm has been chosen, so that the simulator made thicker the mesh elements only where necessary instead of uniformly increase them. Another trick to help the convergence of the results is to set up the simulator for refining the mesh several times more in the y-axis than in the x-axis because of the thin layers present in the geometry. From Tab. 1.2 it is possible to gather that the capacitance tends to convergence as the degrees of freedom

Table 1.2: Simulation results of the IME 50-pair fingers using different amounts of mesh elements. Only the overhanging air has been simulated, the results have been multiplied for $\epsilon_{air} + \epsilon_{glass}$ to estimate the total capacitance.

Degrees of freedom	C_{total} [pF]	K [m^{-1}]
103×10^3	15.44	4.41
226×10^3	15.99	4.26
489×10^3	16.36	4.16
1.04×10^6	16.57	4.11
2.20×10^6	16.70	4.08
4.60×10^6	16.77	4.06

Table 1.3: Simulation results with different numbers of fingers but using a similar number of degrees of freedom normalized to the amount of fingers.

	5 pairs	10 pairs	50 pairs
Degrees of Freedom	611×10^3	1.41×10^6	5.81×10^6
C_{ext_finger}	0.212 pF	0.212 pF	0.215 pF
C_{int_finger}	0.325 pF	0.320 pF	0.328 pF
$C_{total\_simulated}$	1.53 pF	3.00 pF	16.36 pF
$C_{total\_derived}$	1.52 pF	3.09 pF	16.29 pF

(that depend on the amount of elements) grow, so, for this complex geometry, it is not worth to exceed the amount of one million.

Instead of use the whole cross section of the sensor, simplified geometries with only 5 or 10 pairs of fingers has been also simulated. In addition to the total capacitance, the individual capacitances of the internal and external fingers have been verified to find out the equation that generalize the overall value with the amount of fingers. The results are reported in Tab. 1.3 and it can be noticed that the external fingers have a different influence than the internal ones so they have to be distinctly handled. The $C_{total\_derived}$ has been computed using the following equation:

$$C_{total\_derived} = C_{int\_finger} \cdot (n_{pairs} - 1) + C_{ext\_finger} \,, \tag{1.20}$$

that permits to generalize the behaviour regardless the number of fingers. Only

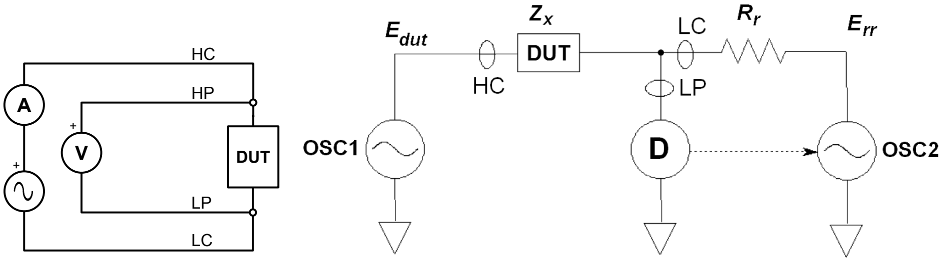

(a) *Four-wire connection: High Potential (HP), High Current (HC), Low Potential (LP) and Low Current (LC).*

(b) *Auto balancing bridge configuration.*

Figure 1.10: The measurement method.

one finger is considered *external* because at the opposite side the external finger is connected to the other branch and so it should not be taken into account.

1.3 Measurement bench

1.3.1 Instruments and methods

The method used for the impedance measurements is the so called **four-terminal sensing** [29]. This technique, excluding the parasitic contributions of the connection cables, provides more accurate measures. This connection is shown in Fig. 1.10(a): the ammeter is placed in series with the generator while the voltmeter measures the potential directly across the Device Under Test (DUT).

Instruments for the impedance measurement at low frequencies are commonly based on the **auto balancing bridge** circuit. The simplified circuit is reported in Fig. 1.10(b): when an excitation signal (OSC1) is applied to the DUT, the Detector (D) forces another signal generator, OSC2, to modify its output for zeroing the potential on the low terminal of the DUT. When this condition is achieved, the unknown impedance can be estimated as:

$$\frac{E_{dut}}{Z_x} = \frac{E_{rr}}{R_r} \rightarrow Z_x = \frac{E_{rr}}{E_{dut}} R_r \,. \tag{1.21}$$

The instruments used for the measurements are:

1. Hewlett Packard 4284A Precision LCR Meter (20 Hz to 1 MHz with fixed predetermined steps);
2. Solartron 1260 Impedance / Gain-Phase Analyzer (10 µHz to 32 MHz with resolution down to 10 µHz).

The first one is a simple impedance meter so the arrangement of the four connectors is plain. On the contrary, for the second one it should be paid more attention because six connectors are present on the front panel. The reason for this higher complexity is due to the possibility of using the instrument for measuring the response of a circuit to a sine wave stimulus. For impedance measurements, the *GENenerator OUTPUT* and the *CURRENT* input play the role of HC and LC terminals, respectively, of Fig. 1.10(a), while the *HI* and the *LO* connectors of *Voltage 1* are the HP and the LP terminals.

The accuracy of the instruments is provided from the user manuals in different ways. For the HP 4284A it is possible to calculate the accuracy as:

$$Er_{acc} = A_e + A_{cal}\,, \tag{1.22}$$

where A_e is the *relative accuracy* and the A_{cal} is the *calibration accuracy* reported in a chart at page 9-20 of the HP 4284A operation manual [30]. A_e, in turn, is made of:

$$A_e = \pm[A + (K_a + K_{aa} + K_b + K_{bb} + K_c) \cdot 100 + K_d] \cdot K_e\,, \tag{1.23}$$

where, for a sample measure at 120 kHz with 100 mV of amplitude on a DUT of (23 + 9i) mS in standard conditions:

- A (*Basic Accuracy*) = 0.1;
- K_a (*Impedance Proportional Factor*) $= 100 \cdot 10^{-6}$;
- K_{aa} (*Cable Length Factor B*) = 0;
- K_b (*Impedance Proportional Factor*) $= 204 \cdot 10^{-6}$;
- K_{bb} (*Cable Length Factor C*) = 1;
- K_c (*Calibration Interpolation Factor*) $= 300 \cdot 10^{-6}$;
- K_d (*Cable Length Factor E*) $= 1.75 \cdot 10^{-3}$;
- K_e (*Temperature Factor*) = 1.

Each coefficient has a corresponding formula or table in the operation manual.

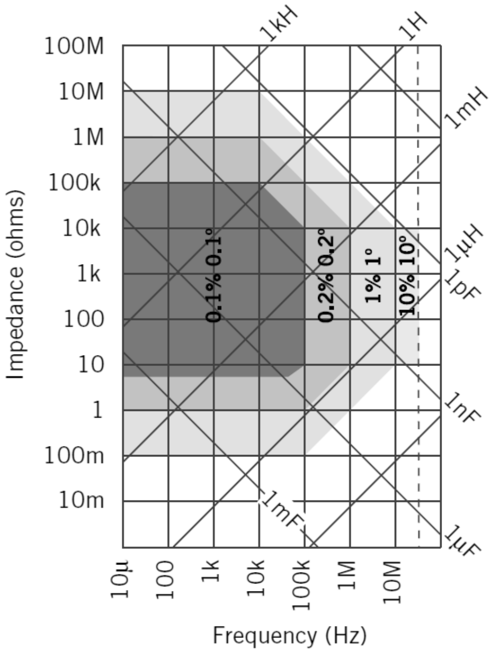

Figure 1.11: Solartron impedance accuracy chart.

With the same conditions, $A_{cal} = 56 \cdot 10^{-3}$, and the total relative accuracy results $Er_{acc} \simeq 0.2\%$.

Instead, for the Solartron 1260, the accuracy is reported in a chart and depends only on the frequency and the impedance of the DUT. That chart is shown in Fig. 1.11.

1.3.2 System block diagram and initial connections setup

The measurement system is able to sequentially measure three samples using one impedance meter only. The two different instruments allows a comparison of the measures for verifying possible configuration mistakes or instrument-dependent behaviours.

The block diagram of the system is reported in Fig. 1.12. The four cables of the impedance meter (LCR meter) are connected to a switch unit that alternately connects one of the three sensors; these sensors, dipped in the samples, are placed in a climatic chamber and, when an accurate temperature

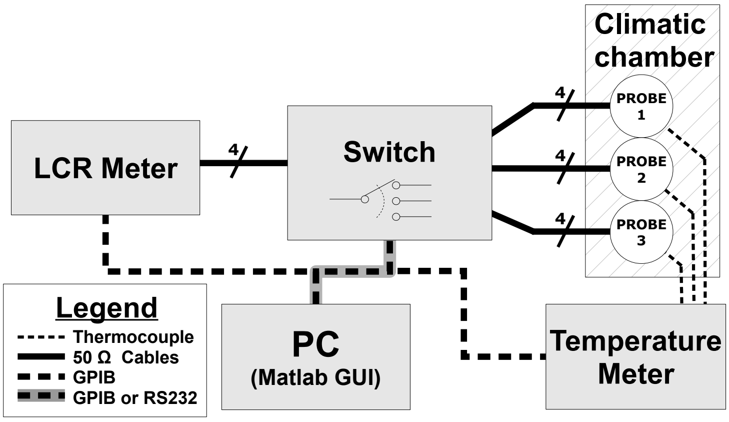

Figure 1.12: Block diagram of the measurement system. For the connection between the computer and the switching unit two kind of interfaces are possible depending on the switch used (see the next subsection).

control is required, the samples are also dipped in a water bath placed in the chamber as well. The temperature of the three samples is measured by means of three thermocouples placed close to each sensor.

The whole system is controlled by a computer through a IEEE-488 GPIB and a RS-232 serial bus. The software has been written in a MATLAB environment creating a GUI (Graphical User Interface) that allows to completely configure the measurements and even a scheduling for long running time measurements (see Appendix A for more information).

For the electrical connection between the four 50 Ω cables and the probes a special connector has been designed, some pictures are reported in Fig. 1.13. Firstly the four cables, after the switch, are soldered to an ARLON25 PCB (Printed Circuit Board) expressly shaped for connecting the cables in pairs and making the two contact points available. The pads of the sensor are contacted through two elastically deformable thin strips of copper soldered on the PCB, shown in Fig. 1.13(a), mechanically pressed on the sensor itself. Everything is held together using two pieces of Teflon and a plastic screw that allows to adjust the force of the contact. The picture of the complete connector is shown in Fig. 1.13(b).

The initial set-up of the connections is based on the AGILENT 34970A

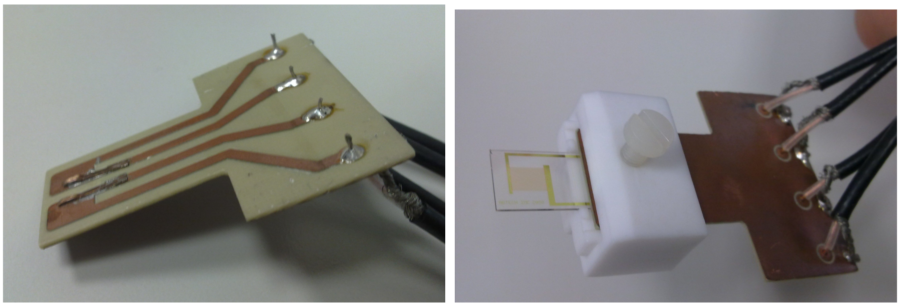

(a) *The PCB board shaped for connect the probes.* (b) *The whole connector that, pressing the probe against the PCB, provides the electrical contact.*

Figure 1.13: The connector used for electrically connect the sensor.

Data Acquisition/Switch Unit with the optional 34901A 20-Channel Multiplexer module. That instrument allows the switching between the three probes changing the states of some relays. Note that the available module does not have coaxial connectors so simple unshielded cables have been used. In Fig. 1.14 the exact wiring configuration is illustrated, each cable from the impedance meter is switched between the corresponding wires connected to the three sensors.

1.3.3 Preliminary tests and improvements

Once the set-up of the measurement bench was completed, initial measurements on the sensor in air have been done. The resulting capacitance at low frequencies was about 190 pF indicating some problems in the system. Several tests in different conditions have been performed and three main issues have been pointed out:

- the unshielded cables, used for the connection of the switch unit, interrupt the shielded paths of the signals and the impedance-controlled lines, this adds about 35 pF to the sensor's capacitance;
- the shieldings connection to earth, carried out through the impedance meters, is interrupted before the switch unit, the coaxial cables connected to the probes are only connected to each others but they are left floating,

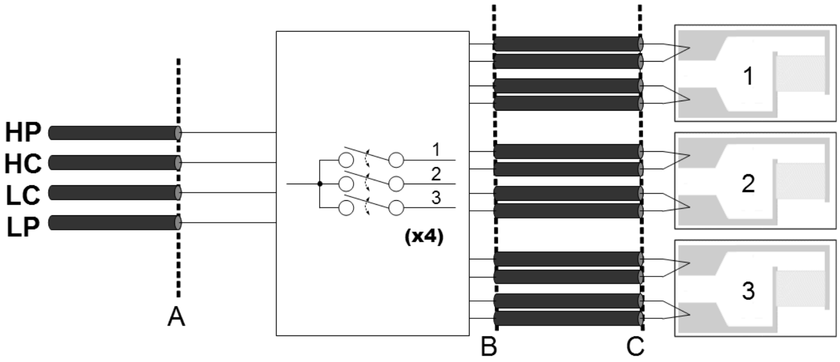

Figure 1.14: Initial set-up of the switching unit based on the Agilent 34970A Data Acquisition/Switch Unit.

thus nullifying any effect of the shielding, and increasing the parasitic capacitance of about 70 pF;

- as already said, the general purpose switch unit affects the measurements with additional 70 pF.

Other tests have been done for verifying different configurations for the shieldings of the coaxial cables that, referring to Fig. 1.14, have to be connected in C (see Fig. 1.13(b)) and also in A and in B.

Consequently a new switching board has been designed for this purpose. On this board four BNC connectors are placed for the impedance meter side while the coaxial cables of the probes are directly soldered next to the relays. The signal lines are designed in order to have an equal electrical path for each sensor, with a controlled 50 Ω characteristic impedance; in addition the analogic part of the board has been electrically isolated from the digital control part. This switch board, hereafter the *MuxBoard*, has a RS-232 serial interface using a Modbus protocol, and allows to select one of the three available sensors. The on-board microcontroller just translates the received instructions into the real command for the relays.

For the actual switching DPDT (Double Pole Double Throw) double winding latching relays have been chosen. This entails several advantages:

- there are different reels, set and reset, for connecting or disconnecting each wire;

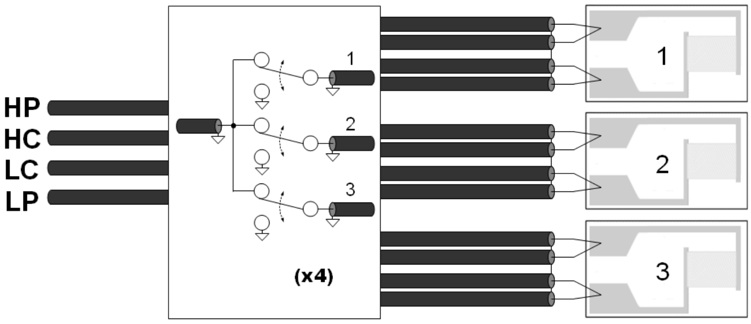

Figure 1.15: Final connection setup of the switching unit based on the designed MuxBoard.

- it is not necessary to keep the reels excited after the commutation, with an appreciable noise reduction;
- the double throw (DT), ensures that the sensors' cables, when not connected to the instruments, are short circuited to ground;
- the same reel operates on two different switches, since they are double pole (DP), thus simplifying the circuit.

The final configuration of the connections is shown in Fig. 1.15 in which it is possible to notice the improved shielding. With this new set-up, the measured capacitance of a probe in air is about 16.7 pF with a cell constant of $4.080\,m^{-1}$, very close to the theory.

Another issue occurred during the preliminary tests was the reliability of the system at high frequency. When the system based on the Solartron 1260 was used for characterizing a $50\,\Omega$ SMD resistor, it shown a resonance above 10 MHz, making the measurements meaningless over that frequency. Note that for this test the instrument was directly connect to the resistance through coaxial cables without any switches or connectors. This effect can be corrected only reducing the cables length. In Fig. 1.16 the effect of a reduction from 1 m to about 10 cm is reported. Since in our first system the cables cannot be shorter than 1 m, measurements will be upper bounded to 10 MHz.

This is not applicable with the HP 4284A, because of its limitation to 1 MHz.

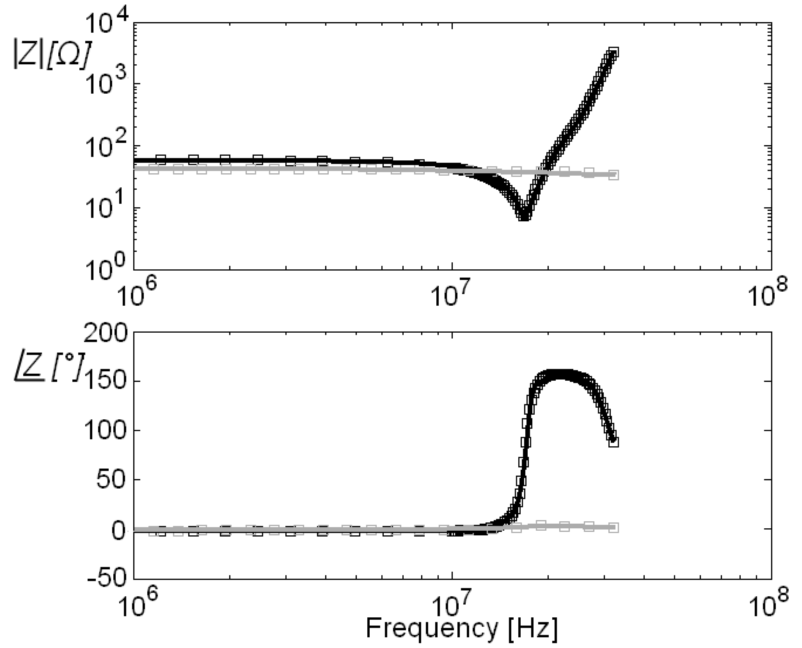

Figure 1.16: 50 Ω resistor measurement results. Black line refers to 1 m long cables. Grey line refers to 10 cm long cables.

1.4 Measurement results

The estimation of electrical parameters, by means of the cell constant, is not so direct when emulsions and polar solutions are measured. Moreover the double layer affects the measured values partially hiding the contribution of the solution in the low frequency range. Therefore, measurements were usually performed in a wide frequency range, analysing impedance and admittance in polar or linear planes, as real and imaginary parts, or as Cole-Cole plots. Secondarily, experimental data were used for obtaining, by complex interpolation, an equivalent circuit model.

The complex interpolation is a common practice in electrochemistry for better separating different contributions. The most difficult step is to find an equivalent electrical circuit, that agrees with data, in which each element could describe a physical phenomenon occurring in the electrode-interface-electrolyte

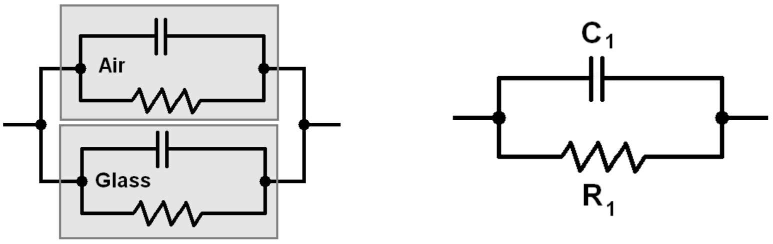

(a) *The complete equivalent circuit.*

(b) *The simplified equivalent circuit.*

Figure 1.17: Equivalent circuit of IDAM in air.

system. As an example, let considering the circuit reported in Fig. 1.17(a), showing the electrical model of the sensor in air: both air cover and glass substrate can be modelled by a RC circuit, but it is not possible to separate the contribution of the superstrate from that of the substrate until the conductivity and the permittivity of one of them are known. For instance, with an air cover and referring to Fig. 1.17(b), experimental data point out for $R_1 = 41\,\mathrm{G\Omega}$ and $C_1 = 16.7\,\mathrm{pF}$ that, considering the specified values of $\epsilon_{glass} = 6.7$ and $\epsilon_{air} = 1$, allows obtaining $R_{glass} = R_1$ ($\sigma_{glass} \gg \sigma_{air}$) and $C_{glass} = 14.5\,\mathrm{pF}$.

Notice that the equivalent circuit should be carefully chosen, having in mind the physical phenomena, and not exceeding in complexity. Circuit model parameters were always extracted from measures in a wide range of frequencies, so that different physical phenomena could be separated. The use of a high number of measures provides an overdetermined system, and correlation coefficients allow evaluating the interpolation accuracy.

LEVM [32] is the Complex Nonlinear Least Square (CNLS) fitting program used for the numerical post-processing. This application needs an equivalent circuit with the initial value of each element and provides the interpolated results, together with several coefficients about the fit quality.

To speed up the post processing stage, several MATLAB scripts have been written in order to display measurement results in different ways and also to automatically interpolate them onto predefined circuits.

In the following section, the most relevant results will be shown together with the interpolations, when needed. Each measurement has been repeated using at least two sensors and in different times. In the reported plots, only one set of measures is shown for clarity and, unless differently indicated, different repetitions gave always similar trends.

However, reproducibility has always been the main challenge because of the non-homogeneousness of milk.

1.4.1 DC measurements

DC measurements are important for deciding the signal level for the following measurements. As already explained in the first part of the chapter, the behaviour of a metal-electrolyte interface is non-linear, schematizable by a pair of two antiparallel diodes, and non-linear phenomena should be avoided since difficult to unravel; therefore the signal level should be limited to the nearly linear area next to zero.

For this test, a direct connection between the interdigitated sensor and a Keithley 2400 SourceMeter was set up and the probe was dipped in full fat milk at about 23 °C.

Fig. 1.18(a) shows the I-V results. Notice that the capacitive nature of the electrode-electrolyte interface leads to long transient times: when a voltage value is applied to the probe, the settling time is of several seconds (Fig. 1.18(b)). Thus, the current was always sampled with a certain delay with respect to the voltage steps. It should be also reminded that the DC current, established after a constant voltage application, is due to the faradaic resistance in parallel to the double layer capacitor.

The interpolation with the exponential Bulter Volmer equation (Eq. 1.12), gives the following values:

$$I = I_s \cdot (e^{\frac{V}{\eta V_T}} + e^{-\frac{V}{\eta V_T}}) = 18 \times 10^{-9} \cdot (e^{\frac{V}{0.32}} + e^{-\frac{V}{0.32}})\,. \tag{1.24}$$

Observe that the interface capacitive behaviour is responsible for the non-zero current with null voltage, and that the direction of such a current depends on the polarity of the last potential applied. This can be explained considering the long discharge transients caused by the double layer.

After these first measurements it was decided to use always a signal level less than 300 mV. To confirm such a conclusion, some impedance measurements have been done on the full frequency range with different amplitudes of the excitation voltage. The results are shown in Fig. 1.19 and point out an alteration of the milk characteristics at low frequency for amplitudes higher

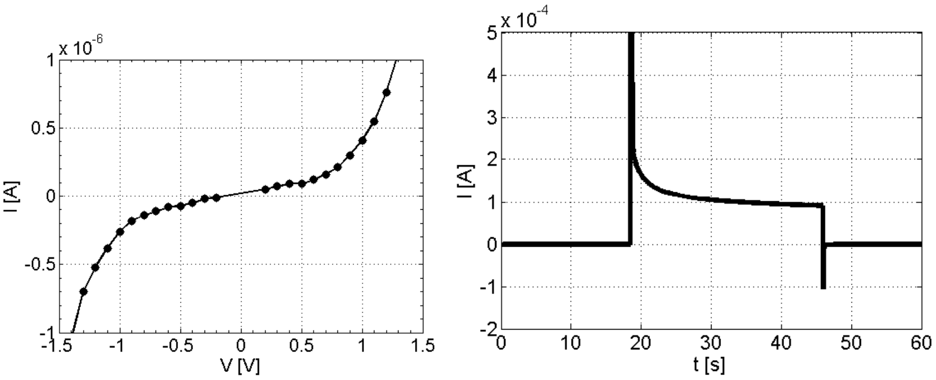

(a) *DC characteristic.*

(b) *Long transient responses.*

Figure 1.18: I-V measurements on milk. After each voltage change, a short delay is necessary before measuring the current for settling.

than 500 mV_{rms} for the modulus of the admittance, and over 300 mV_{rms} for its phase. At high frequency no relevant effects have been observed because of the slowness of the involved kinematics.

Hereafter, 100 mV_{rms} will be always the excitation amplitude.

1.4.2 Water conductivity

Distilled water has been used as a first conductivity experiment for its plainness and well known characteristics. The nominal value of the conductivity of ultra-pure water reported in literature is about 5.5 µS/m with samples of pure water that can be even of higher magnitude.

For our analysis two different samples of distilled water have been used: a sample provided by the clean room of the Information Engineering Department and a bi-distilled sample of the Department of Chemistry. Experimental results are shown in Fig. 1.20.

In this case, the equivalent circuit should include a series conductance G_{water} accounting for water conductivity σ_{water}, a series capacitance C_{dl} describing the double layer effect and, in parallel, the capacitance due to substrate, C_{glass}. Notice that C_{dl} is present, since some dissociate ions were present in our samples, as can be gathered by the measurement results.

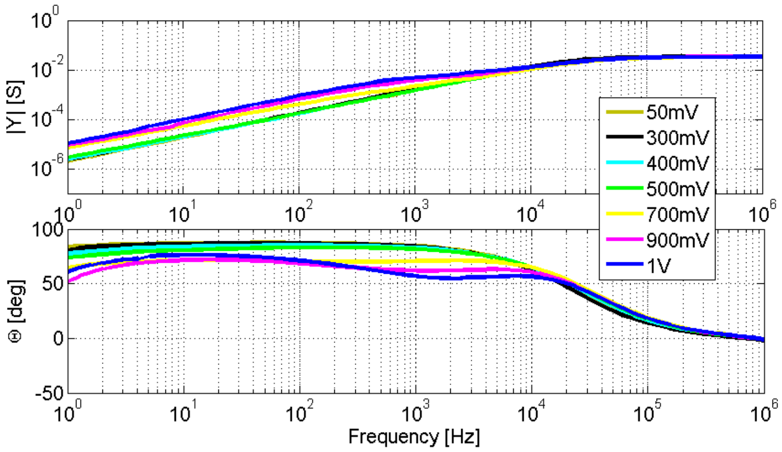

Figure 1.19: Modulus and phase of the admittance for several amplitudes of the excitation voltage applied to a sensor dipped into a milk sample. The reported amplitude should be intended as rms.

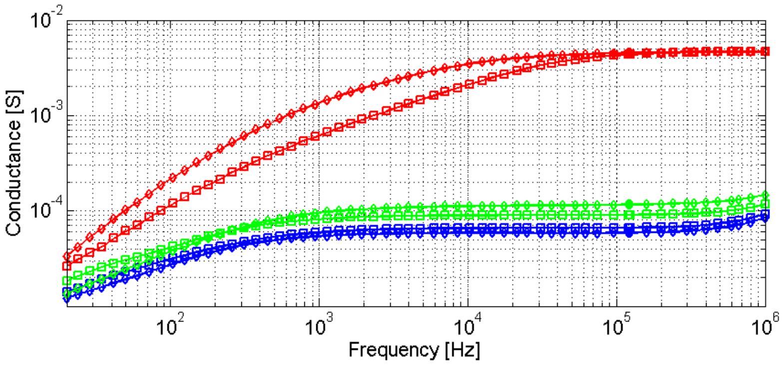

Figure 1.20: Real part of the admittance measured for three different samples of water: distilled water from the clean room of the Information Engineering Department (blue), distilled water from the Department of Chemistry (green), and drinking water (red). Each measurement has been repeated two times.

The total admittance can be expressed as:

$$
\begin{aligned}
Y &= j\omega C_{glass} + \frac{G_{water} \cdot j\omega C_{dl}}{G_{water} + j\omega C_{dl}} \\
&= j\omega C_{glass} + \frac{G_{water}^2 \cdot j\omega C_{dl} - G_{water} \cdot \omega^2 C_{dl}^2}{G_{water}^2 + \omega^2 C_{dl}^2} \,,
\end{aligned}
\tag{1.25}
$$

so that,

$$
\Re\{Y\} = -\frac{G_{water} \cdot \omega^2 C_{dl}^2}{G_{water}^2 + \omega^2 C_{dl}^2} \,. \tag{1.26}
$$

Comparing Eq. 1.26 with Fig. 1.20 it should be noticed that the plot can be divided in two parts:

1. **low frequencies :** for $\omega \to 0$, $\Re\{Y\} \to 0$, the faradaic resistance is very high in distilled water, so that it was not considered;
2. **middle-high frequencies :** for $\omega \to \infty$, $\Re\{Y\} \simeq G_{water}$, allowing the extraction of the σ_{water}:

$$
\sigma_{water} = G_{water} \cdot K \,. \tag{1.27}
$$

Finally, notice that, when the admittance modulus is considered, two different zones con be distinguished in the middle-high frequencies:

2a. **middle frequencies :** for intermediate frequencies $G_{water}^2 \ll \omega^2 C_{dl}^2$ and $\omega C_{glass} \ll G_{water}$ so that $Y \simeq G_{water}$; $C_{dl} \gg C_{glass}$ ($\epsilon_{water} \sim 80 \gg \epsilon_{glass} = 6.7$);

2b. **high frequencies :** for $\omega \to \infty$, $Y \to \infty$ because the glass capacitance short-circuits the probe.

Tab. 1.4 reports the estimated conductivity of these samples along with samples of a commercial mineral water. Nominal and measured values of the mineral water well agree. The available samples of distilled water allows only a qualitative comparison: they were obtained by laboratories of our university and were reasonable characterized by a conductivity well higher than that which can be obtained in the state-of-the-art semiconductor of pharmaceutical clean rooms. Notice that these measured values are important because the same water will be used for the following tests.

Table 1.4: Nominal and measured conductivity of different kinds of water.

Water type	Nominal Conductivity	Estimated Conductivity
Drinking water	19.5 mS/m	18.7 mS/m
Clean Room water	-	~ 0.20 mS/m
Chemistry Dep. water	-	~ 0.32 mS/m
Ultra Pure water	5.5 µS/m	-

1.4.3 Conductivity of standard solutions - OIML R56

The international standard for the conductivity measurement is based on potassium chloride solutions. In the OIML R56 [33] International Recommendation, complete instructions for preparing samples with predetermined conductivities are reported.

The samples have been prepared using the distilled water of the clean room and the KCl salt has been weighed with an accuracy of ±3 mg. Five samples, with molar concentrations of 1M, 0.1M, 0.01M, 0.005M and 0.002M, have been prepared following the quantities reported in the standard; others samples, with lower KCl quantities, have been derived from the 0.01M sample with subsequent dilutions for increasing the accuracy.

The results are reported in Fig. 1.21 for a fixed frequency of 1 MHz. It is noticeable a very slight underestimation for low concentrations, while a remarkable saturation appears for values higher than 0.01M. This effect can be explained considering the pole in Eq. 1.26, which is $\omega_p = G_{water}/C_{dl}$, and moves its position toward higher frequency when the conductivity of the solution grow. The knee at low frequency in Fig. 1.20, shifts to higher frequency, shifting also out of the instruments capability the flat region where it is possible to measure the conductivity .

Complex interpolations in a wide frequency range were also performed, but no sensible improvements were obtained with respect to the direct evaluation at one fixed frequency. For that reason, a more complete review of the applicability of this technique is postponed to the following section.

1.4.4 Measurements on vaccine milk

After these initial measurements, IDAM sensors were applied to more complex solutions. Vaccine milk has been chosen since it is one of the most important

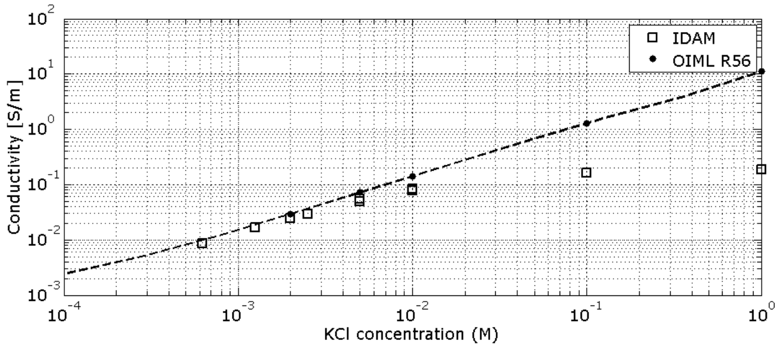

Figure 1.21: Conductivity of several KCl solutions at 1 MHz compared with the values reported in the standard [33].

Table 1.5: Main constituents of cow milk with average percentages. [34]

Water	Protein	Lactose	Fat	Salts
87 %	3.6 %	4.9 %	4 %	0.7 %

food in daily life, adulterations and contaminations lead to economical losses, and should be important to perform rapid and simple quality tests during the processing.

The approximate composition of cow milk is reported in Tab. 1.5. Components percentage is variable depending on the cow breed, diet and even season.

Some studies have been done on the effects of the milk composition on its conductance, [13, 20], but quantitative conclusion is not available yet.

The classical electrical model of Fig. 1.22(a), reported in literature [13, 14, 15, 16], agrees with the one used before for water. For a better modelization of the double layer it is possible to introduce the *Constant Phase Element*, CPE. That component is a pure theoretical element, without any real correspondence with an electronic element, and its impedance is defined as:

$$Z_{CPE}(j\omega) = \frac{1}{T \cdot (j\omega)^{\phi}}\,, \tag{1.28}$$

where T is a scale factor and ϕ is associated to a phase shift ranging from 90 °

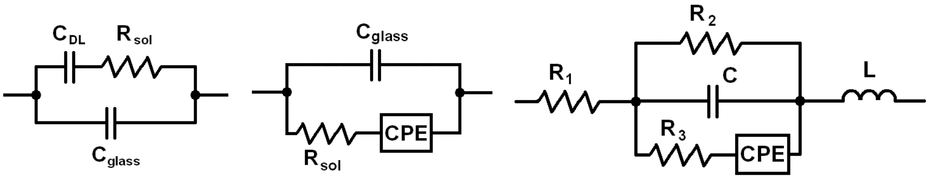

(a) *Classical model.* (b) *Adopted model.* (c) *Example of useless, too-complex circuit.*

Figure 1.22: Equivalent circuits of the milk impedance useful for the complex interpolation of the data.

when $\phi = 1$ (capacitive behaviour) to 0 ° when $\phi = 0$ (resistive behaviour). This peculiarity is very useful because milk shows, in the low frequency range, an admittance phase of about 83 °, which cannot be accurately modelled by standard elements only.

In Fig. 1.22(b) the adopted circuit model is shown, in the following data interpolations C_{glass} (due to glass substrate contribution) is considered constant, $C_{glass} = 14.5\,\text{pF}$. Notice that such a circuit is only one of the possible electrical models that can be used for interpolating the experimental data. Other circuits, perhaps more complicated as that shown in Fig. 1.22(c), might be used but with a questionable advantage in turns of accuracy comprehension of the associate physical phenomenon.

The results of several tests will be shown in the following pages to investigate the environment contribution. It should be reminded again that milk is an emulsion and the measurement reproducibility is affected by this characteristic. Some tests were done for improving the reproducibility, for instance by stirring the samples with a magnetic stirrer or by waiting a given time after dipping. Only slight improvements were obtained against a high increase of the set-up complexity, so these attempts were given up. UHT milk was used for the most part of the experiments, since it is better characterized and more stable. Some measurements onto full-fat fresh milk were also performed for comparison and no relevant differences were noticed.

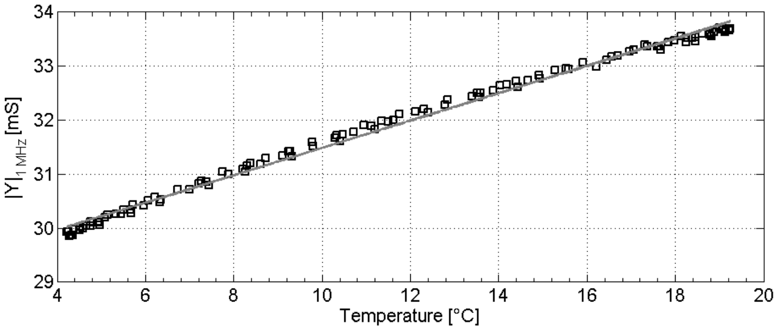

Figure 1.23: Admittance at 1 MHz as a function of temperature. Both experimental data (marker) and linear interpolation (line) are shown.

1.4.4.1 Temperature influence

Temperature is the environmental factor that most influence the electrical parameters. As an example, a 5 °C drift has an effect sensibly larger than the adulteration with a significant percentage of water.

For this test two samples of milk were placed in a climatic chamber programmed for executing several consecutive thermal cycles from 4 °C to 20 °C. The probes, dipped in the samples for the whole experiment, have been measured at regular intervals of 20 minutes, together with the milk temperature, measured by two thermocouples. The test lasted more than 40 hours, so possible ageing effects have been monitored, comparing the measures obtained in successive thermal cycles.

As it is possible to notice in Fig. 1.23, a linear trend with a slope of about 0.25 mS/°C has been found at 1 MHz. From the analysis of the real and the imaginary part of the admittance, it comes out that such behaviour depends on the conductance, since susceptance just exhibits a drift in the initial thermal cycle. Conversely, at low frequency, the imaginary part alone changes with temperature with an initial drift.

Using a standard expression for linear trends, the relation between admittance and temperature can be expressed as:

$$|Y| = Y_{4C} \cdot (1 + x \cdot (T - T_0)), \tag{1.29}$$

where Y_{4C} is the modulus of the admittance at the temperature $T_0 = 4\,°\mathrm{C}$ while x is the thermal coefficient equal to $0.0087\,(°\mathrm{C})^{-1}$.

Table 1.6: Fat content of different kinds of milk for 100 ml.

Milk type	Fat quantity
Full-Fat	3.60 g
Semi-skimmed	1.55 g
Skimmed	0.10 g

1.4.4.2 Fat content

The commercial milk is commonly classified depending on the thermal processes used and on its fat content. The fat content of the main kinds of milk is reported in Tab. 1.6.

Measurements have been done in order to verify possible admittance differences between three different samples of milk but no clear modifications were pointed out. As expected [13], the conductance of skimmed milk was higher, but only in the shown frequency range of Fig. 1.24 and not at lower and higher frequencies. The same behaviour is confirmed at different temperatures and also with different delays between the dipping instant and the measurement time. A delay of almost few minutes is needed before measurement results become stable, probably because of the diffusion process and the electrokinetic reaction at the electrode-electrolyte interface. Notice that the required delay depends on the dilution of the solution, decreasing for more diluted emulsions.

1.4.4.3 Milk sophistication with water addition

Water addition is the most common sophistication in milk trade. Not evident effects appear for small percentage of water and, even with complex techniques, it is not always possible to quantify the adulteration.

Commercial mineral water has been chosen as adulterant in our experiments instead of distilled water, chosen in [13, 14, 15, 16], since this seems to be a more realistic scenario of adulteration.

Sensitivity is at its maximum in a range between few hundreds of kilohertz and few megahertz. Fig. 1.25(a) shows the admittance at 1 MHz as a function of the fraction of added water. Measurements were carried out at room temperature, approximatively at 23(2) °C. Another test, with controlled temperature, has been performed and will be reported later. Data can be interpolated by a

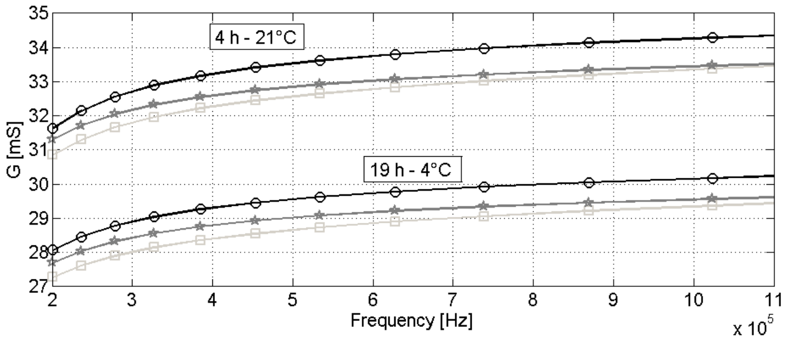

Figure 1.24: Conductance from about 200 kHz to 1 MHz for three different kinds of milk: skimmed (circles), semi-skimmed (stars) and whole or full-fat milk (squares). Two different series of data are shown, one at 21 °C, obtained after 4 hours, and the other at 4 °C, measured after 19 hours.

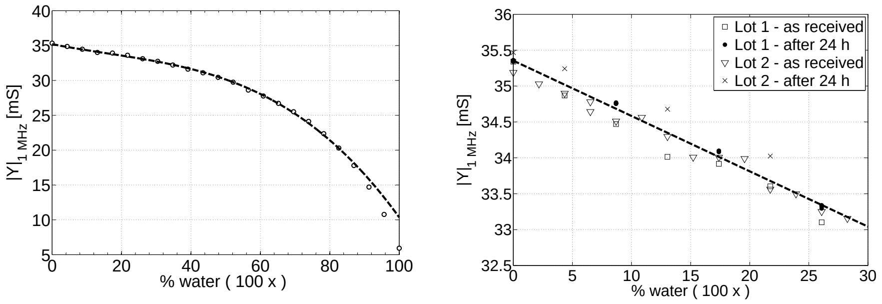

(a) *Full view.*

(b) *0% - 30% Range.*

Figure 1.25: Admittance as a function of the fraction of water added to UHT milk at 23 °C. In (b) some measurement repetitions are also reported. Lines refer to polynomial interpolations of the 3rd order for the full range of adulteration (a) and of the 1st order for small fractions of adulterant (b).

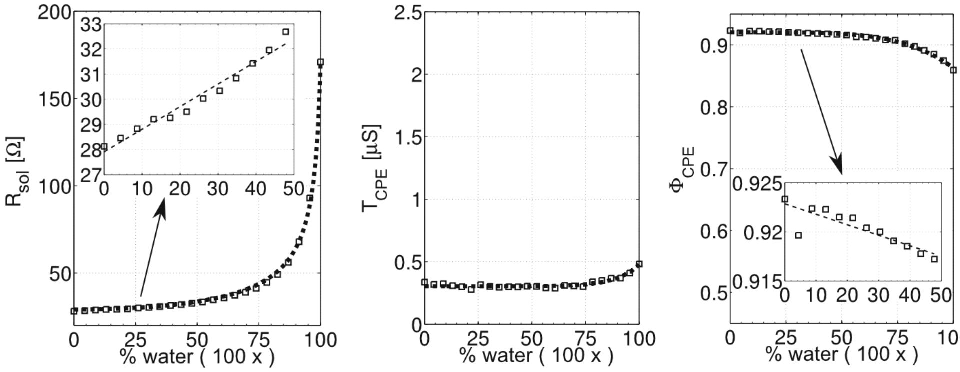

(a) R_{sol}.
(b) T_{CPE}.
(c) Φ_{CPE}.

Figure 1.26: The modification of the elements of the equivalent circuit with the water addition.

3rd order polynomial

$$|Y| = p_3x^3 + p_2x^2 + p_1x + p_0\,, \tag{1.30}$$

$$|Y| = (-2.88 \times 10^{-2})x^3 + (1.37 \times 10^{-2})x^2 + (-9.78 \times 10^{-3})x^3 + (3.52 \times 10^{-2})\,. \tag{1.31}$$

For small-medium amount of water the behaviour is almost linear (see Fig. 1.25(b)), and this was confirmed by repeating measurements in different times and by using samples by different lots of milk. Measurement sensitivity can be increased by means of complex interpolations of the measures onto the equivalent circuit of Fig. 1.22(b). The obtained results are reported in Fig. 1.26. It should be noticed that such values were obtained through the complex interpolation over a wide frequency range and that they are not referred to one specific frequency only.

As seen above, at medium-high frequencies, the solution resistance related to the milk conductance, R_{sol}, is the dominant element on the admittance, so a similar behaviour to that reported in Fig. 1.25(a) can be found for $1/R_{sol}$ (see Fig. 1.26). R_{sol} starts from about $29\,\Omega$ (milk resistance, R_{milk}) and ends to about $170\,\Omega$ (water resistance, R_w) for water only samples. Dividing this late value by the cell constant of the probe and inverting the result, a water

Table 1.7: Interpolation parameters A, B and C in equations (1.32), (1.33) and (1.34). ρ represents the regression coefficient.

	R_{sol}	Φ	T
A	102	0.92	0.30
B	4.64	2.69	7.79
C		$3.79 \cdot 10^{10}$	$8.58 \cdot 10^{15}$
ρ	0.999	0.994	0.953

conductivity of about 233 µS/cm, very close to the nominal value of 235 µS/cm, was obtained. The electrical parameters can be interpolated by the following functions:

$$R_{sol} = R_{milk} + \left(\frac{1}{\sqrt{1 - \left(\frac{x}{A_{R_{sol}}} \right)^2}} - 1 \right) \cdot \frac{R_w - R_{milk}}{B_{R_{sol}}}, \tag{1.32}$$

$$\Phi_{CPE} = A_\Phi \cdot e^{-\frac{(x)^{B_\Phi}}{C_\Phi}}, \tag{1.33}$$

$$T_{CPE} = A_T \cdot 10^{-6} \cdot e^{\frac{(x)^{B_T}}{C_T}}, \tag{1.34}$$

where the coefficients are reported in Table 1.7.

With respect to the sensitivity which can be obtained by considering the admittance at 1 MHz only (Fig. 1.25(b): 0.22 (mS/mS)/x), the sensitivity given by the relative variation of R_{sol} due to the water fraction x, improves up to 0.32 (Ω/Ω)/x. This demonstrates that the electrical model provides more information.

The same measurements were repeated on fresh milk. Experiments were performed placing all the samples in the climatic chamber at a set point of 5 °C. Before measuring a sample, this was moved into the water bath, placed in the climatic chamber as well. Notice that, the water bath was at a temperature slightly higher than the set point, typically at 9 °C, since during the operations performed for changing the samples and cleaning the sensors, the door of the climatic chamber remains open for some minutes, and the average temperature of the chamber increased.

The sample temperature was therefore monitored until the measurement temperature of 8.5 °C was reached and, at that point only, the impedance

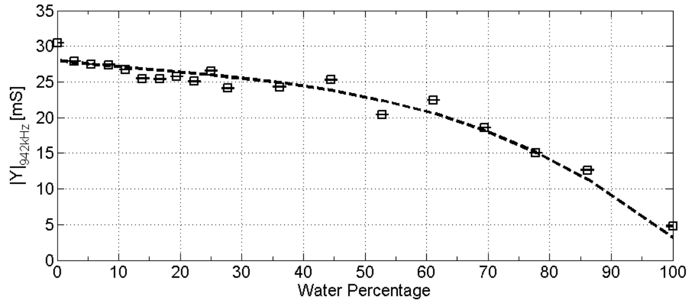

Figure 1.27: Admittance as a function of the fraction of water with respect to pure fresh milk samples at 8.5 °C. The horizontal bars on the squares represent the possible temperature effect. The interpolation line found with room temperature measures on UHT milk is reported for comparison (dashed line).

was measured. Further temperature variations during the measurements were acquired and used coherently with Eq. 1.29. In Fig. 1.27 the new results are reported and compared with the interpolation line of Eq. 1.31 (only the initial value p_0 has been modified). This apparent agreement suggests a good repeatability of the overall behaviour, with the exception of the increased standard uncertainty, probably due to the inhomogeneity of the fresh milk.

1.4.4.4 Milk contamination with ammonia

Ammonia is a constituent of several cleaning products used in diary industry. When the machines used for the milk processing are cleaned, some traces of ammonia can remain inside the pipes and contaminate the milk. The quantities should be extremely limited so only few ppm (part per million) of ammonia were added to milk samples in order to check the sensitivity to this contaminant. A 5% solution of ammonia was used, since higher concentrations are dangerous and, so, not easily achievable.

Measurements were repeated two times on the same samples showing a high level of uncertainty with respect to the effect induced by the ammonia. In Fig. 1.28(a) measurement results on dilutions from 1 ppm to 1000 ppm are reported, pointing out a weak leaning toward higher admittance values. If we consider the electrical parameters after a complex interpolation, Fig. 1.28(b), the uncertainty is so high that it is difficult to extract some useful information.

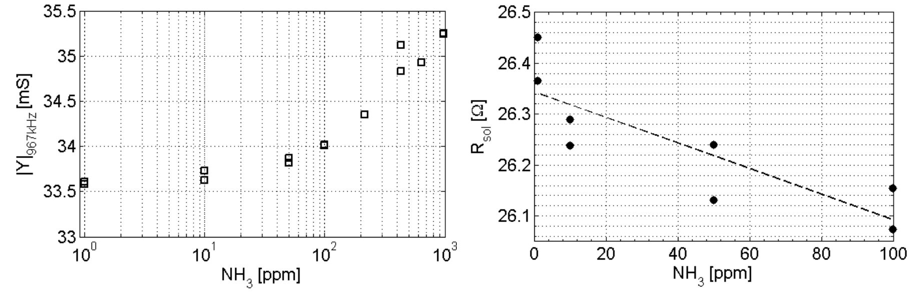

(a) *Admittance value.* (b) *Interpolation results for R_{sol}.*

Figure 1.28: Solution admittance and modelled solution resistance as a function of ammonia percentage.

Notice that, since a diluted solution of ammonia was used, water amount increased together with ammonia, so that, because of its opposite effect on the overall admittance, the two contributions counteract.

1.4.4.5 Milk contamination with benzalkonium chloride

Benzalkonium chloride is commonly used as disinfectant in diary industry so, like with the ammonia, some residual can contaminate the milk. The highly-dense solution used for the test was at the 50% of concentration, and four samples were obtained by mixing milk with this solution in percentage ranging from 130 ppm to 1000 ppm.

The measured admittance was not correlated with the percentage of solution and so, to verify the correctness of the measurement procedure and since the electrical parameters of the benzalkonium were not available, we performed some tests with distilled water instead of milk. The results are reported in Fig. 1.29 showing a clear indication of the increasing quantity of biocide added to the samples.

In conclusion it is possible to affirm that benzalkonium chloride is easily detectable in distilled water but the presence of the several constituents of the milk, together with their interaction with the biocide, hide the admittance variation making the benzalkonium detection with this simple technique not possible.

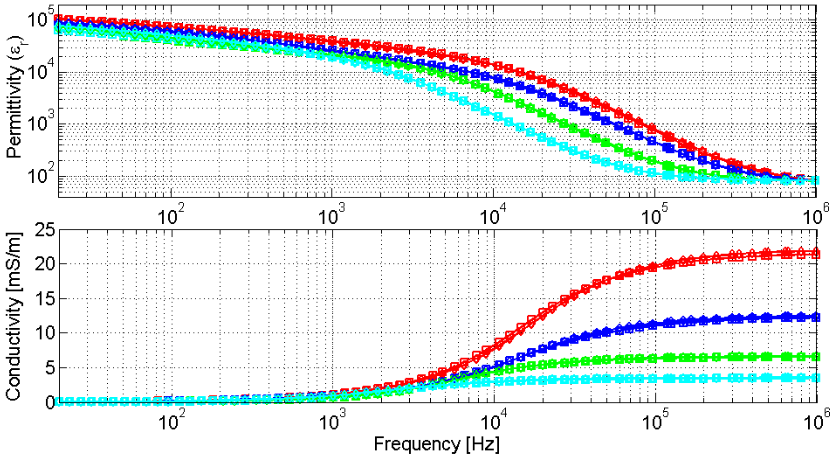

Figure 1.29: Permittivity and conductivity measured on four different samples as a function of frequency. In the four samples 1000 ppm (red), 519 ppm (blue), 260 ppm (green) and 130 ppm (light blue) of benzalkonium chloride were added to the distilled water.

CHAPTER 2

Variable Electrochemical Cells with Parallel Plate Sensors

One of the most critical issue in the impedance spectroscopy of biological samples, is the double layer on the electrode-electrolyte interface. At low frequency, such layer masks the effective impedance of the solution, and a correct interpretation of the results becomes more difficult.

A method for separating the interface and the bulk contributions is proposed in [35]. This technique is based on a parallel plates geometry specifically modified for moving one plate and so allowing measurements with different electrodes gaps. The electrolyte bulk contribution can be obtained from the measurement results by measuring the impedance between the plates, with the solution under test placed in the gap, for different gaps.

In Fig. 2.1(a) a schematic representation of the sensor, with an electrolyte placed between the plates, is shown: two double layers with charged ions are formed close to the plates, while the central part represents the bulk. An equivalent circuit is reported in Fig. 2.1(b), where the interface impedance is named as Z_{int}. It is not important to represent it with circuital elements, like a CPE, as done in the previous chapter. The bulk resistance and the bulk capacitance are defined as:

$$R_{bulk} = \frac{d}{\sigma_{bulk} \cdot S}\,, \qquad\qquad C_{bulk} = \epsilon_0 \epsilon_{r_{bulk}} \frac{S}{d}\,, \tag{2.1}$$

where d is the distance between the plates, S is the area and σ_{bulk} and $\epsilon_{r_{bulk}}$

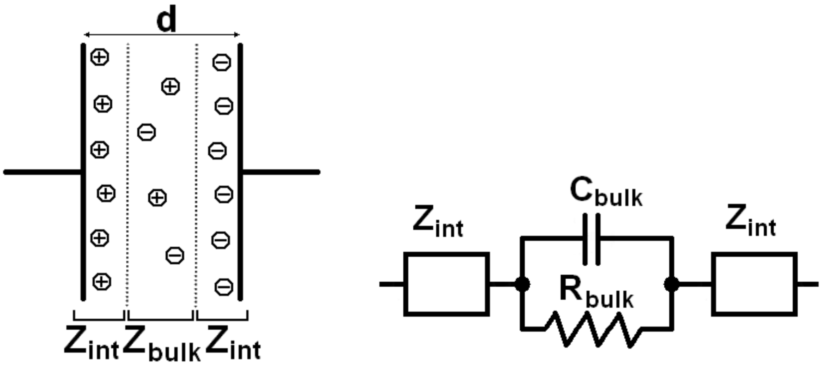

(a) *Schematic representation.* (b) *Equivalent circuit.*

Figure 2.1: Parallel plates sensor representation.

are the sought solution's conductivity and permittivity, respectively.

This technique is based on the fundamental hypothesis that the impedance of the double layers does not depend on the distance between the plates of the sensor. Under such hypothesis, when the plate distance is modified, the impedance variation can be ascribed to Z_{bulk} only, so that σ_{bulk} and $\epsilon_{r_{bulk}}$ can be estimated by using the impedance values measured for at least two different distances d.

The analytical approach was modified with respect to the one reported in [35], with the aim of obtaining an exact solution.

Referring to Fig. 2.1(b), the total measured impedance is equal to:

$$Z_m = Z_{int} + Z_{bulk} + Z_{int} = Z_{int}^{'} + Z_{bulk} \, , \tag{2.2}$$

in which the two interface contributions have been combined. The bulk impedance, in turn, can be expressed as:

$$\begin{aligned}
Z_{bulk}(j\omega) &= \frac{R_{bulk}}{1+j\omega R_{bulk}C_{bulk}} \\
&= \frac{R_{bulk}}{1+\omega^2 R_{bulk}^2 C_{bulk}^2} - j\frac{\omega R_{bulk}^2 C_{bulk}}{1+\omega^2 R_{bulk}^2 C_{bulk}^2} \\
&= \frac{\frac{d}{\sigma_{bulk}S}}{1+\frac{\omega^2 d^2 \epsilon_0^2 \epsilon_{r_{bulk}}^2 S^2}{\sigma_{bulk}^2 S^2 d^2}} - j\frac{\frac{\omega d^2 \epsilon_0 \epsilon_{r_{bulk}} S}{\sigma_{bulk}^2 S^2 d}}{1+\frac{\omega^2 d^2 \epsilon_0^2 \epsilon_{r_{bulk}}^2 S^2}{\sigma_{bulk}^2 S^2 d^2}} \\
&= \frac{1}{\sigma_{bulk}\left[1+\delta^2\right]}\frac{d}{S} - j\frac{\delta}{\sigma_{bulk}\left[1+\delta^2\right]}\frac{d}{S}\,, \qquad (2.3)
\end{aligned}$$

where $\delta = \omega\epsilon_0\epsilon_{r_{bulk}}/\sigma_{bulk}$.

Therefore, the measured impedance can be written as:

$$Z_m = \left(\Re\{Z_{int}^{'}\} + \frac{d}{\sigma_{bulk}\left[1+\delta^2\right]S}\right) + j\left(\Im\{Z_{int}^{'}\} - \frac{\delta d}{\sigma_{bulk}\left[1+\delta^2\right]S}\right)\,. \qquad (2.4)$$

As it is possible to see from Eq. 2.4, both the real and the imaginary part of the measured impedance, linearly depend on the distance d between the sensor's plates. Consequently, it is possible to obtain the slopes of the functions $\Re\{Z_m(d)\}$ and $\Im\{Z_m(d)\}$ from two measurements at different distances. These slopes, respectively

$$m_{\Re\{Z_m\}(d)} \triangleq m_r = \frac{1}{\sigma_{bulk}\left[1+\delta^2\right]S}\,, \qquad (2.5)$$

$$m_{\Im\{Z_m\}(d)} \triangleq m_x = -\frac{\delta}{\sigma_{bulk}\left[1+\delta^2\right]S}\,, \qquad (2.6)$$

allow obtaining the electrical parameters σ_{bulk} and $\epsilon_{r_{bulk}}$:

$$\sigma_{bulk} = \frac{1}{S\left(m_r + \frac{{m_x}^2}{m_r}\right)}\,, \qquad (2.7)$$

$$\epsilon_{r_{bulk}} = -\frac{\sigma_{bulk} m_x}{m_r \omega \epsilon_0}\,. \qquad (2.8)$$

It can be also noticed that the y-intercepts of the two functions are the real and the imaginary part of the interface impedance respectively.

In the following sections, two prototypes will be presented , together with the obtained results.

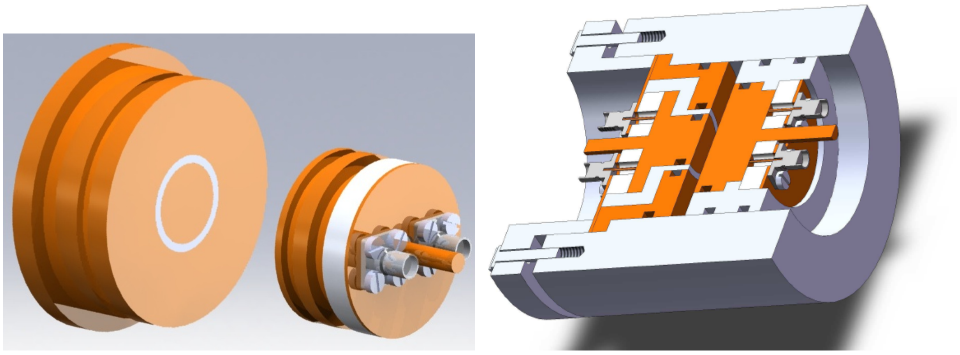

(a) *Facing plates.*

(b) *The cylindrical chamber in section with the plates placed in the measurement position.*

Figure 2.2: The first prototype. The colours indicate the material used: brass for the orange parts and white for the not conductive ones. The plate on the left in the figures is the fixed one while the movable one, on the right, is reported without the external sleeve of Teflon.

2.1 First prototype

A closed electrochemical cell has been designed and realized following the geometry used in [35]. The liquid under test is confined in a cylindrical chamber which is closed by two metal discs that act as electrodes. One disc has a protruding edge that locks the plate position to a fixed height, and the other one is free to slide inside the cylinder. The fixed plate has been divided in a central disc with a 20 mm diameter, used as a sensing element, and in an annular ring, the *guard ring*, that acts like a shield around the central disc (see Fig. 2.2). Let note that the sensitive area is limited to the central disc even if the movable plate is larger than the fixed one.

The sensor is composed by several parts, some of brass and the others of Teflon, fitted together to allow a correct electrical connection. Referring to the section reported in Fig. 2.2(b), there are two SMA connector for each plate, the shielding is connected to the external side of the plates while the signal wires connect the interior side through some thin pins stuck into the plates.

Two grooves have been arranged between the parts that should hold the liquid, for the housing of two O-rings. Similarly, two O-rings have been placed between the movable plate and the external chamber, to ensure a better seal and greater flowingness.

Each plate has a pivot, directly connected to the internal disc, that allows an accurate control of the movable plate position inside the cylindrical chamber and makes easier the disassembly.

The presence of two SMA connectors for each plate allows performing a *four-terminal* interconnection for the impedance measurement [29], as already done with the IDAMs in the previous chapter.

The electrochemical cell has been mounted in a mechanical structure with the purpose of easily handling the device. The key element of such structure, reported in Fig. 2.3, is a *micromanipulator* that allows an accurate control of the movements in the cylinder direction. This device has a resolution of 10 µm on a range of about 20 mm. Some blocks, composed by not-conductive material, have been designed for mechanically connecting the pivot of the movable plate to the micromanipulator. A pin has been used as lock element for a quick disassembly of the cell. Finally the cell is placed on a special support and fixed using two metal strips.

Two holes have been dug out in the top and bottom of the chamber for refilling and emptying the cell, a small tank has been also placed on the upper hole to ensure a complete filling.

2.1.1 Cell calibration

The first test was made without any liquid in the chamber in order to verify the mechanical behaviour of the sensor in well defined conditions. The measurements were done starting with a null distance between the plates (electrical short) and moving them away. This test was initially performed without the O-rings for having better mechanical sensitivity, and the results are shown in Fig. 2.4. The expected behaviour in air is purely capacitive with values derived from the geometrical sizes of the sensor

$$C = \epsilon_0 \epsilon_r \frac{S}{d} \rightarrow C^{-1} = \frac{d}{\epsilon_0 \epsilon_r S}\,, \tag{2.9}$$

where $\epsilon_r = 1$ (air) and $S = (0.01^2 \cdot \pi)\,\mathrm{m}^2$. When this curve was plotted together with the experimental results against d, two error contributions were observed:

1. **a different slope**, which can be ascribed to an incorrect estimation of the effective area S of the plates;

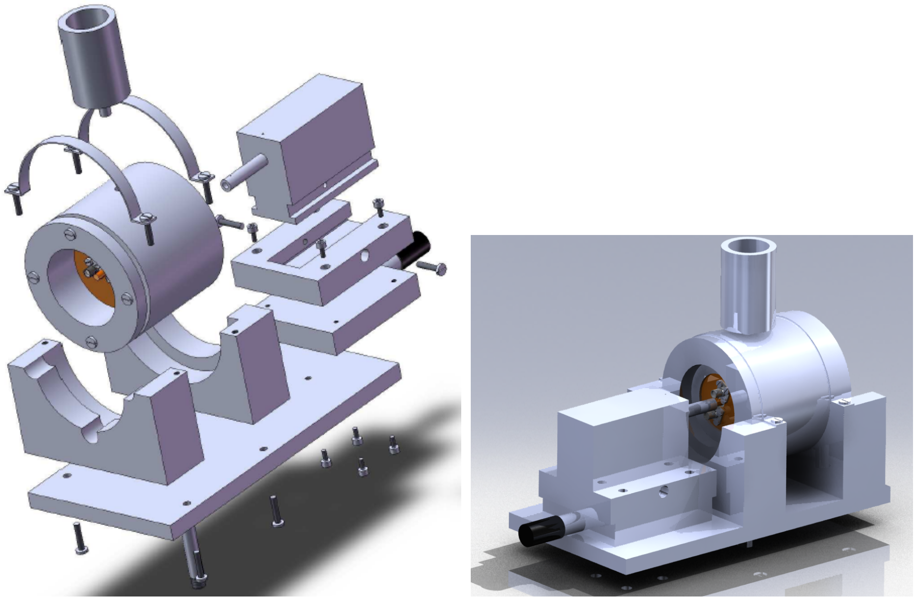

(a) *Exploded system.* (b) *Complete system view.*

Figure 2.3: The device complete of the mechanical handling.

2. **an offset error** with respect to the nominal electrode-to-electrode distance. In effect it was not so easy to find the zero position, which changes every time the cell is reassembled.

It is possible to include these errors, modifying the Eq. 2.9

$$C^{-1} = \frac{d + d_{err}}{\epsilon_0 \epsilon_r \left[S \left(1 + \frac{S_{err}}{S} \right) \right]}\,, \tag{2.10}$$

where S_{err} and d_{err} quantify these two contributions.

Finally, the effective area of the electrodes, $S_{eff} = (0.0111^2 \cdot \pi)\,\mathrm{m}^2$, was obtained from the measured impedance values while for the *zero distance*, d_{err}, a new calibration was made at each reassembly.

The relative error in the area was $\sim 11\%$, and was partially due to the manufacturing tolerance and to the edge effects. Fig. 2.5 reports the results of

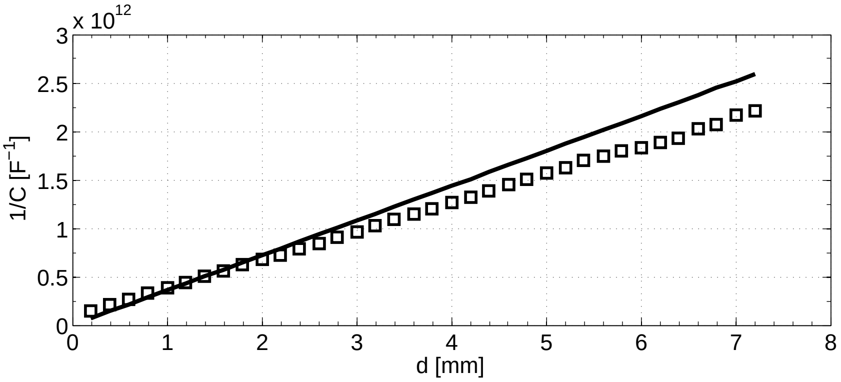

Figure 2.4: Experimental results in air (squares) compared with the expected values (solid line).

Table 2.1: Comparison between expected and measured values.

Sensor	Isolation	S_{eff}
Expected value	-	$(0.01^2 \cdot \pi)\,\mathrm{m}^2$
PPS1	2 mm	$(0.0111^2 \cdot \pi)\,\mathrm{m}^2$
PPS1 modified	0.3 mm	$(0.0102^2 \cdot \pi)\,\mathrm{m}^2$

some FEM simulations, it is evident that some electrical field lines reach the lateral faces of the underneath disc through the insulator placed between the sensing area of the fixed plate and the shielding, so that not only the facing area contributes to the overall capacitance.

Edge effects were partially removed by reducing the space between sensing and shielding areas. This reduction was obtained by designing a PCB, *Printed Circuit Board*, with a better definition of the sensing and shielding elements, covering and connecting the fixed electrode through some pins, as shown in Fig. 2.6(a).

In this way, the isolation between the conductive areas could be reduced from ∼2 mm to ∼0.3 mm. A new effective area $S_{eff} = (0.0102^2 \cdot \pi)\,\mathrm{m}^2$ was so obtained as reported in Tab. 2.1 and shown in Fig. 2.6(b).

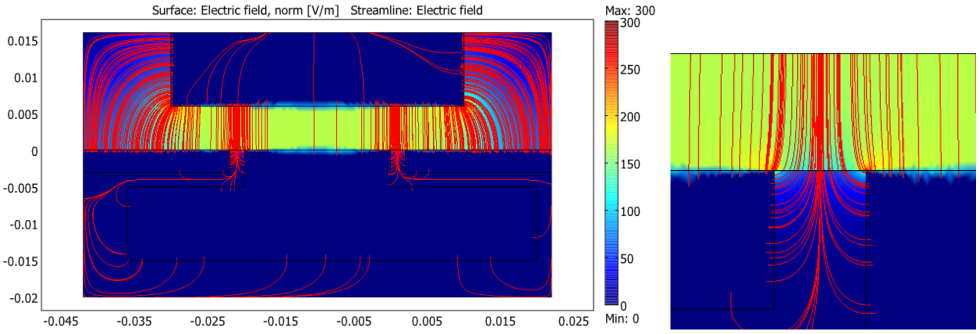

(a) *Section view.*

(b) *Edge effect.*

Figure 2.5: FEM simulation of the edge effect.

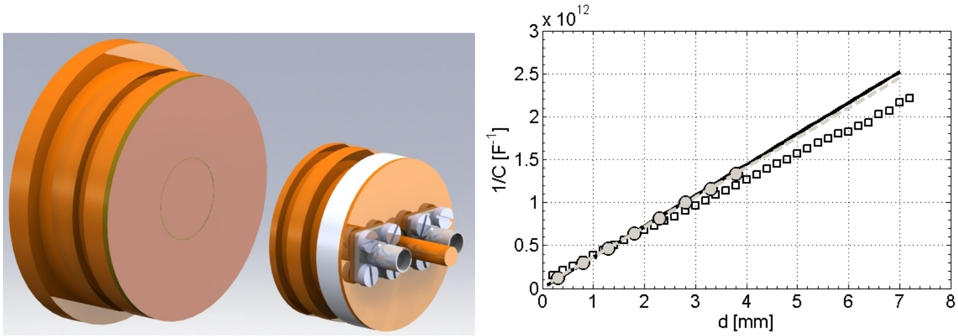

(a) *The PCB applied on the fixed plate.*

(b) *Results obtained with the modified version (circles) and their interpolation (dashed line) compared to the expected values (solid line) and the initial version (squares).*

Figure 2.6: Modified electrode and measurement results.

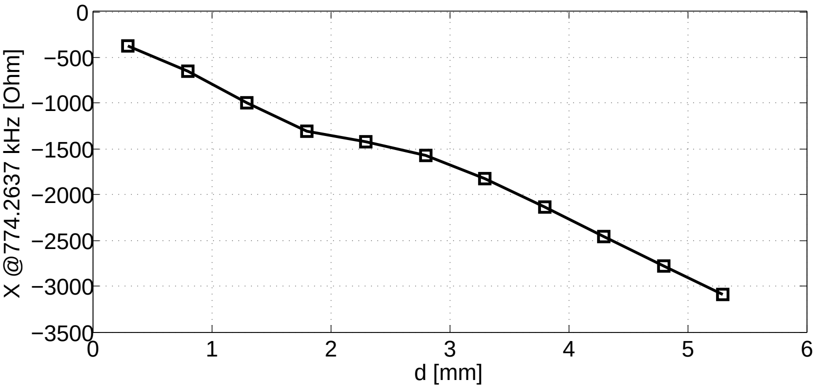

Figure 2.7: Reactance values as a function of the distance d when distilled water was inserted in the cell.

2.1.2 Preliminary measurements results

Distilled water was chosen for the initial realistic tests of the first prototype. The O-rings were inserted for sealing and the distance between the electrodes was reduced until the two plates contact each other, several measurements were done moving away the movable plate through the micromanipulator.

The measured impedance is mainly imaginary for a dielectric as the distilled water, and should have approximatively a linear behaviour with the distance between the plates:

$$\Im\{Z_m\} = -\frac{1}{\omega C_{water}} + A = -\frac{d}{\omega \cdot \epsilon_0 \epsilon_{r_{water}} S_{eff}} + A\,, \tag{2.11}$$

where the constant A depends both on the double layer contribution and on the residual error in the estimation of d.

The experimental values of the reactance X of Fig. 2.7 show an apparent hump at a distance of about 2 mm indicating some problems in the measurement setup. The same test was repeated several times, reassembling the whole structure, and the same behaviour appeared in each experiment. The effective displacement of the movable part was directly measured with a calliper, finding out that the movable plate does not correctly follow the shift for distances of about 2 mm, even if the micromanipulator appeared correctly settled. An increasing strain of the micromanipulator was noted at that distance, and this

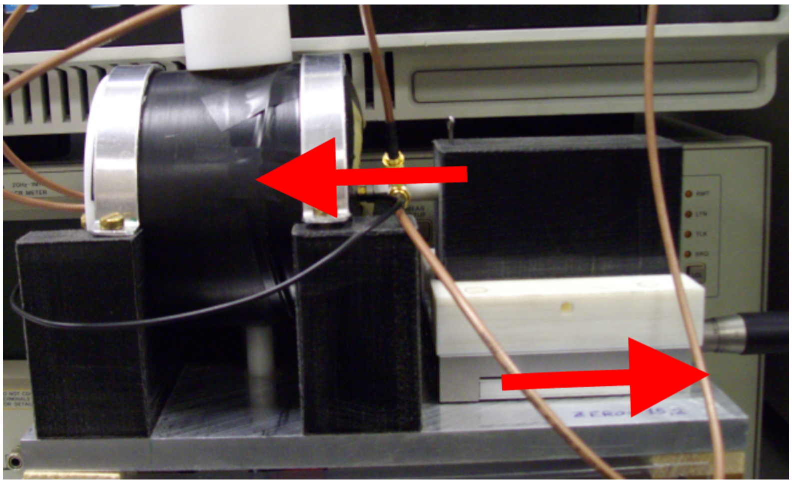

Figure 2.8: The set up during a measurement. The red arrows indicate the direction of the shear stress applied to the mechanical support.

indicated that a slight mechanical distortion of the parts caused the difference between true and nominal position values. Fig. 2.8 shows a picture of the sensor with the stresses.

These stresses were due to the O-rings, which hindered a correct sliding movement, because of the friction coefficient of the insulating material and the mechanical tolerances. In fact, when the movable plate was pushed against the fixed one, the O-rings tended to remain next to the furthest side of the grooves with respect to the sensing surface. Moving away the plates, the O-rings easily slid toward the opposite side of the grooves thanks to the low friction coefficient of the Teflon for the few first millimetres. Afterwards, continuing to moving away, the O-rings slid against the internal walls of the chamber (made of nylon) producing high friction and deforming the support of the micromanipulator. When the stress became high enough to move the movable plate of the sensor, the structure resulted not deformed anymore and the real shift corresponded again with the set value of micromanipulator (see Fig. 2.8).

Finally, since the use of thinner O-rings for reducing the friction impeded the water-tightness, the external O-rings were removed and the movable plate was enclosed in a flexible membrane sealing the chamber. This allowed an extremely low friction, but the sensor needed a complete disassembly after

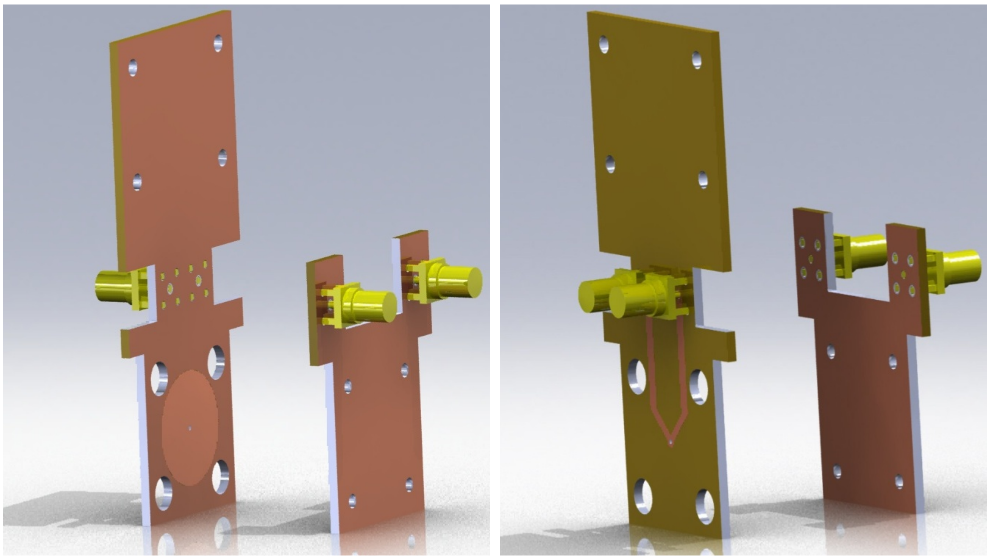

(a) *Front view.*

(b) *Rear view.*

Figure 2.9: The PCBs used as fixed (on the left) and movable (on the right) plate of a parallel plate configuration. The rear view is reported for showing the electrical connection with the SMA connector.

each measurement for removing the liquid and cleaning the surfaces. Moreover, the membrane needed to be changed very often because of its weakness, and so a second prototype was developed.

2.2 Second prototype

An open geometry was studied to avoid any kind of friction. Two PCBs were used as electrodes and a 20 mm diameter circle was milled on one of them. Two SMA connectors were soldered directly on the each PCB and connected in order to have the same electrical configuration of the first prototype. Fig. 2.9 reports the front and rear view of the designed boards.

The PCB on the left of Fig. 2.9(a) was fixed to the same support element of the micromanipulator. The other PCB was attached to the moving part of the micromanipulator for adjusting the distance of the two electrodes, as

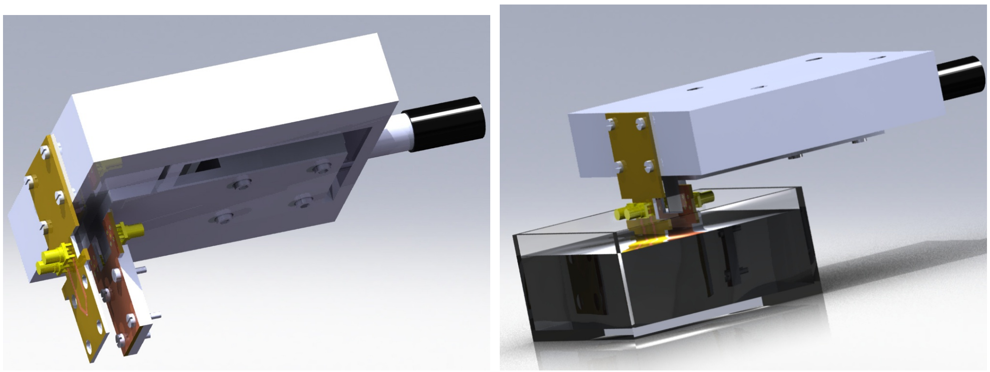
(a) *Complete view.* (b) *Dipping of the plates.*

Figure 2.10: Complete sensor configuration and correct positioning during a measurement.

shown in Fig. 2.10(a).

Finally, the system was dipped into the liquid under test for the measurements as in Fig. 2.10(b).

2.2.1 Calibration

As before, the first measurements were done in air for obtaining the effective area of the electrodes, which resulted $S_{eff} = (0.01009^2 \cdot \pi)\,\mathrm{m}^2$ (Fig. 2.11(a)).

Then, the results obtained with distilled water (Fig. 2.11(b)) showed a linear behaviour which corresponds to the absence of any stress, proving the assembly effectiveness.

2.2.2 Measurement results

Several measurements of standard liquids were done for a complete characterization of the sensor. As an example, the obtained $\sigma_{bulk}(f)$ and $\epsilon_{r_{bulk}}(f)$ of distilled water are reported in Fig. 2.12. Notice that parameters are both constant only between 1 kHz and 100 kHz, as found in [35]. In effect,

- at low frequencies the high impedance of the double layer tends to hide the bulk contribute, making difficult a correct estimation;

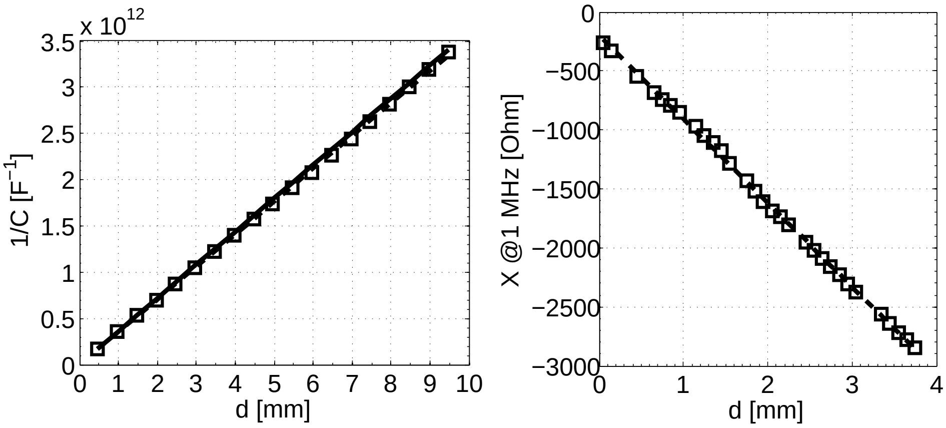

(a) *Measurements in air. Experimental (markers and dashed line) and expected behaviour (solid line).*

(b) *Measurements in water.*

Figure 2.11: Calibration measurements to be compared with those obtained with the first prototype.

- at high frequencies the bulk capacitance decreases its impedance and so the bulk resistance, in parallel to that capacitance, does not concur any more to the measured impedance.

Other results are reported in Tab. 2.2. Only the estimation of the known electrical parameters are shown for each liquid. The conductivity of the water is not shown because the sample was different respect the others used for the IDAMs test so meaningful comparisons cannot be done.

Finally, after these preliminary measurements, the electrochemical cell was used with milk samples, adulterated with different quantities of mineral water. Let consider now the two procedures which were followed:

Procedure A:

1. For a given sample of adulterated milk, remembering that the milk impedance is mainly real, $\Re\{Z_m(f_n, d)\}$ was measured for different values of d and for a single frequency f_n;
2. the conductivity of the bulk solution was obtained from the slopes, by using Eq. 2.7. For instance, the variation

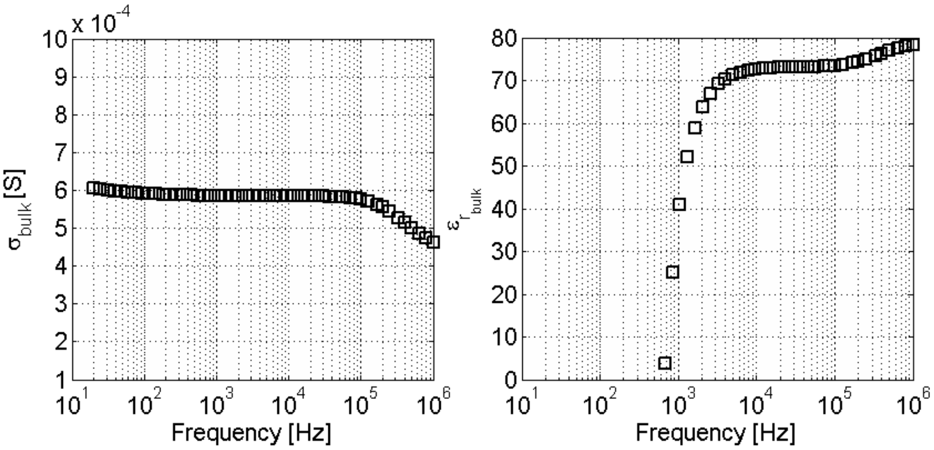

Figure 2.12: Conductivity and permittivity of distilled water, according to Eqs. 2.7 and 2.8.

Table 2.2: Comparison between nominal and measured values for some test liquids.

Solution	Nominal $\epsilon_{r_{bulk}}$	Measured $\epsilon_{r_{bulk}}$
Distilled water	78.5 (@100 kHz, 25 °C)	73.5 (@100 kHz, 23(2) °C)
Isopropyl alcohol	18.3 (@100 kHz, 25 °C)	20.2 (@100 kHz, 23(2) °C)

Solution	Standard OIML σ_{bulk}	Measured σ_{bulk}
KCl 0.01M	0.141 S/m (@25 °C)	0.144 S/m (@1 MHz, 23(2) °C)
KCl 0.001M	0.0147 S/m (@25 °C)	0.0164 S/m (@1 MHz, 23(2) °C)

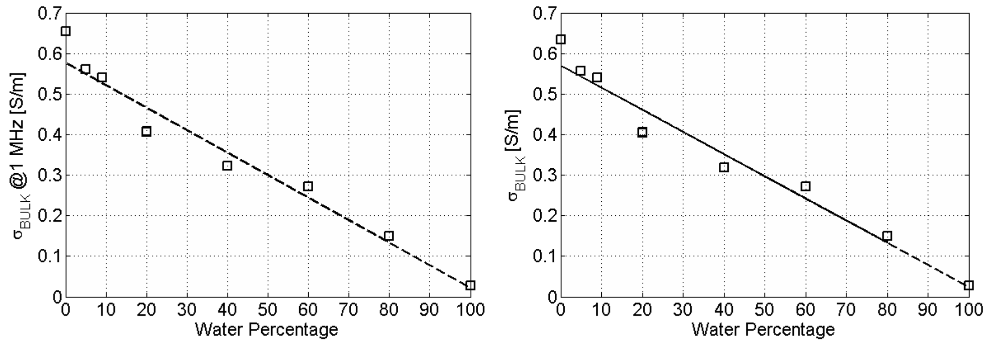

(a) *Procedure A.*

(b) *Procedure B.*

Figure 2.13: Results obtained with milk adulterated by water addition. *Procedure A* is based on a linear interpolation with d on a single frequency measurements. *Procedure B* is based on the equivalent circuit model, which has been obtained from measurements from 20 Hz to 1 MHz.

of σ_{bulk} (f_n $= 1\,\text{MHz}$) with the percentage of added water is shown in Fig. 2.13(a).

Procedure B:

1. For a given sample of adulterated milk, from all frequency values of $Z_m(f, d)$, the equivalent circuit parameters, corresponding to the series of a CPE and a resistance R, were extracted, as in section 1.4, for different positions d;
2. σ_{bulk} was then obtained from $R(d)$ by using Eq. 2.7.

The only difference between the two methods is that the first one is based on the processing of measurements performed at a single frequency, while the second one takes into account the whole frequency range. The results of Fig. 2.13 point out no relevant differences, so in the data processing the complex interpolation does not provide additional information.

Moving on some direct comparisons with the IDAMs sensors, it should be noticed that the variable electrochemical cell can be used down to 100 Hz, even with measurements on milk samples, while IDAMs show useful results with frequencies higher than ~100 kHz only. That can be explained reminding that, for IDAMs measurements, the double layer strongly affects the results,

Table 2.3: Comparison between variable electrochemical cell (PPS) and IDAM sensors. Different procedures have been used to obtain the reported results: linear interpolations on several measures at 1 MHz with different gaps (*Procedure A*) and complex interpolations on the whole frequency range (*Procedure B* and *Interp*).

Sensor and Technique	Drinking water	UHT full-fat milk
Nominal	24.8 mS/m	-
IDAM Interp.	23.1 mS/m	132 mS/m
PPS2 Procedure A	27.4 mS/m	0.65 S/m
PPS2 Procedure B	27.4 mS/m	0.63 S/m

masking the bulk parameters especially at low frequencies.

Some measurement results are reported in Tab. 2.3 showing that correct values are obtained with both the sensors for low conductive solutions only, while, when complex solutions with higher conductivities are measured, IDAMs tend to overestimate the resistivity as seen in the subsection 1.4.3.

No further considerations on the estimations obtained with the electrochemical cell are possible because no reference instruments were available for additional comparisons.

CHAPTER 3

Ultrasound Velocity Sensor

3.1 Basic ultrasounds theory

Ultrasounds are pressure waves which can be propagated in materials, with frequencies ranging from 20 kHz to few hundreds of megahertz. Material sensors based on ultrasonic transducers often measure some wave parameters, since these parameters are strongly dependent on the characteristics of the media the wave is travelling through.

A plane pressure wave that propagates along x-axis can be described by

$$\frac{\partial^2 p(t,x)}{\partial x^2} = \frac{1}{c^2} \cdot \frac{\partial^2 p(t,x)}{\partial t^2}, \tag{3.1}$$

or by its alternating solution

$$p(t,x) = p_0 e^{-\alpha x + j\omega(t - \frac{x}{c})}, \tag{3.2}$$

where p_0 is the wave amplitude in $x = 0$, for $t = 0$, α the spatial attenuation and c the velocity of the ultrasound wave which propagates with the wavelength $\lambda = c/f$.

The speed of propagation c and the spatial attenuation α are specific of the material which the wave propagates in. In detail, for simple liquids:

$$c_{liquids} = \sqrt{\frac{K}{\rho}}, \tag{3.3}$$

with ρ the density of the liquid and K its bulk modulus (i.e. the inverse of the compressibility β). The spatial attenuation on the contrary depends on several contributions: the absorption, the viscous, thermal and scattering losses and the losses due to the relaxation processes; the latter, in turn, depend on other material-specific parameters. More details can be found in [36].

The **acoustic impedance** (Z), that is, approximatively,

$$Z \simeq \rho c \,, \tag{3.4}$$

is another important parameter of ultrasound propagation. In fact, this is a fundamental parameter for understanding the behaviour of the sonic wave at the interface between two different materials. Similarly to the case of electromagnetic waves, an incident pressure wave feeling a discontinuity of the medium, excites two waves: the reflected wave that bounces back in the original material, and the transmitted one that continues the propagation through the new material. The amplitudes of the reflected and the transmitted waves, normalized to the amplitude of the incident wave, are known as the reflection (R) and the transmission (T) coefficients respectively, and can be obtained as

$$R = \frac{Z_2 - Z_1}{Z_1 + Z_2} \,, \tag{3.5}$$

$$T = 1 + R \,, \tag{3.6}$$

where Z_1 and Z_2 are respectively the acoustic impedances of the materials before and after the interface.

As long a pressure wave has to propagate through different materials, a matching network should be found for delivering the maximum power to the load. The matching network can be based on a $\lambda/4$ transformer. As it is well known from the transmission line theory, the impedance seen at the input of a $\lambda/4$ long line with acoustic impedance Z_3 is given by $Z'_{IN} = {Z_3}^2/Z_2$ if Z_2 is the impedance of the load. Therefore, a $\lambda/4$ transmission line of characteristic impedance $Z_3 = \sqrt{Z_1 Z_2}$ matches the load Z_2 and a source with impedance Z_1.

The most critical issue of the matching line is its limited bandwidth, since the layer length is $\lambda/4$ for a specific frequency only and therefore the useful range is limited to a narrow band centred on it. Two subsequent matching layers (Fig. 3.1) can be used for having a more gradual change of the acoustic impedance and so for widening the bandwidth. The impedances at the input

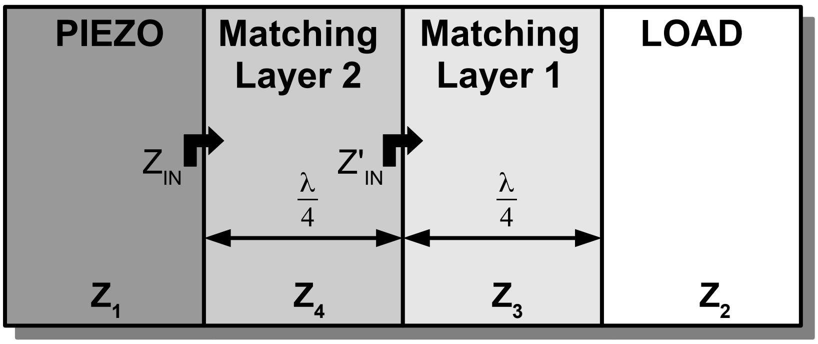

Figure 3.1: Matching technique between materials with different acoustic impedances.

of the first and the second matching layers are, respectively:

$$Z'_{IN} = \frac{{Z_3}^2}{Z_2}\,, \tag{3.7}$$

$$Z_{IN} = \frac{{Z_4}^2}{Z'_{IN}} = \frac{{Z_4}^2 Z_2}{{Z_3}^2}\,. \tag{3.8}$$

It is therefore possible matching a source impedance Z_1 by means of two $\lambda/4$ layers if

$$Z_{IN} = Z_1 = \frac{{Z_4}^2 Z_2}{{Z_3}^2} \rightarrow \frac{Z_1}{Z_2} = \left(\frac{Z_4}{Z_3}\right)^2\,. \tag{3.9}$$

Let now consider that the previous equations are valid for steady conditions only. In fact, during the transients, as the incident wave gets through the first (the second) interface, it instantaneously sees the impedance Z_4 (Z_3, respectively) rather than Z_{IN} (Z'_{IN}). Thus, in the presence of pulsed waves, the previous matching condition is not so useful and can be substituted by the following equations:

$$Z_1 = \frac{{Z_4}^2}{Z_3} = \frac{\left(\frac{{Z_3}^2}{Z_2}\right)^2}{Z_3} = \frac{{Z_3}^3}{{Z_2}^2} \rightarrow Z_3 = \sqrt[3]{Z_1 {Z_2}^2}\,, \tag{3.10}$$

$$Z_1 = \frac{{Z_4}^2}{Z_3} = \frac{{Z_4}^2}{\sqrt[3]{Z_1 {Z_2}^2}} \rightarrow {Z_4}^2 = \sqrt[3]{{Z_1}^4 {Z_2}^2} \rightarrow Z_4 = \sqrt[3]{{Z_1}^2 Z_2}\,. \tag{3.11}$$

Note that these values ensure that the transmission line is matched only during the first wave transit. As the incident wave arrives at load, it is partially reflected since Z_2 does not match Z_3 so that, after a time corresponding to the forwards and backwards travel, the matching condition is lost. For a correct behaviour, the transmitted pulse must finish before that instant, so that it can be convenient to extend the matching layers by an integer number of wavelength.

3.2 State of the art

Ultrasounds are widely used in sensing systems thanks to some attractive features:

- non-invasive measurements, since ultrasounds can pass through covering materials;
- rapid response time, that, together with the previous one, allows in-line utilization;
- low power consumption;
- long term stability;
- high resolution and accuracy.

However, there are some issues about material characteristics and response interpretation:

- substances under investigation must be acoustically conductive or at least not excessively absorbent;
- for some applications, acoustic properties of the substances should be well known;
- response signal needs complex post processing;
- signal corruption due to gas bubbles and attenuation at high-frequency are common problems.

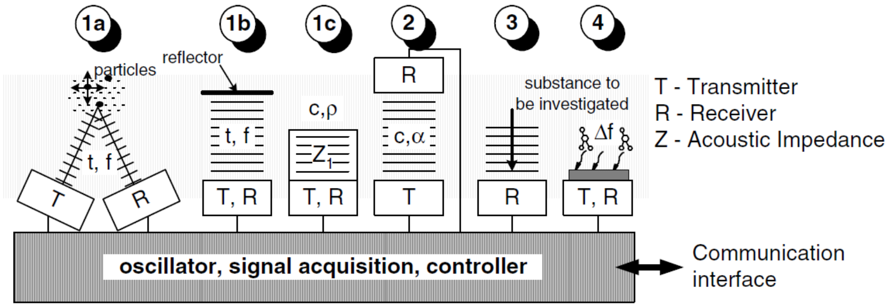

Figure 3.2: Different kinds of ultrasonic sensor systems: velocity meter of particles using Doppler effect (1a), distance meter using phase shift (1b), material characteristics detector using amplitude attenuation (1c) and (2), process monitor sensing ultrasound vibrations (3), element specific detector using resonances (4). See [36].

Several measurement techniques are possible: reflection (1), transmission (2), emission (3), and resonance-based (4). In Fig. 3.2 the correspondent transducers configurations are also shown. The most relevant difference is that, in some cases, when the stimulus and the received signals are temporally spaced, the transmitter can also acts as receiver, as for the (1b), the (1c) and the (4) configurations.

Another difference between the various techniques consists on the used parameter: amplitude or delay. In the first case measurement results will be related to several material properties, which influence the attenuation. In the second one, only the delay between the pulse transmission time and the reception time is taken into account, regardless the signal amplitude.

When the issue is the propagation velocity, i.e. the delay time of the receiver pulse, commonly called *Time of Flight* (TOF), the most important techniques than can be adopted for estimating the arrival-time of the received pulse (see Fig. 3.3) are based on:

1. first arrival-time;
2. threshold-based time [37];
3. first zero-crossing time;
4. cross-correlation [38];

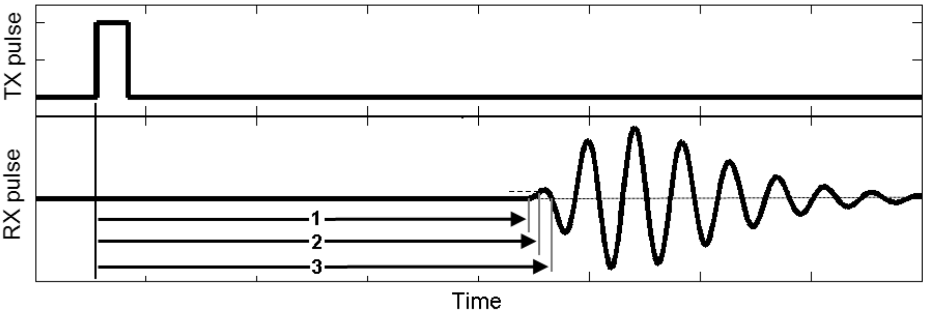

Figure 3.3: TOF estimation using different techniques for the arrival time detection: first arrival-time (1), threshold-based time (2), and first zero-crossing time (3).

5. signal envelope analysis [39].

The first one is practically difficult to implement with good accuracy: the time of arrival is not well defined because of the noise and the small signal amplitude, so that this approach is uncommon. In threshold-based time techniques, the receiver circuit might consist of a single comparator. However, signal amplitude variability and noise should be accounted for, because of their influence on the accuracy. On the contrary, the detection of the first zero-crossing time is less affected by amplitude and noise, at the cost of a more complex post processing. Finally, the last two techniques use all the received signal, but they are usually applied to ultrasound in the lower part of the spectrum, up to ∼100 kHz.

The zero-crossing times following the first one are not generally taken into account, even if they could be less affected by noise and by signal amplitude when the maximum of the signal envelope corresponds to peaks following the first one. However, fully digitized data acquisition offers new possibilities, and the aim of this work is to investigate the possible advantages of using one or more subsequent zero-crossing times for ultrasonic waves of some megahertz.

3.3 System description

A block diagram of the measurement system is given in Fig. 3.4. It consists of:

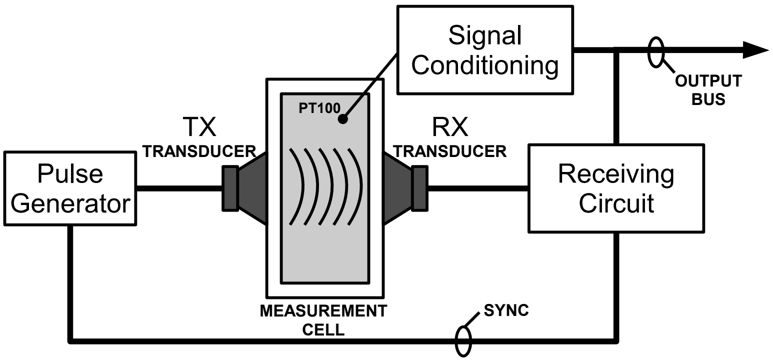

Figure 3.4: Block diagram of the first measurement system for the ultrasound velocity.

1. a transmitting circuit which includes a pulse generator and an ultrasonic transducer;
2. a measurement cell with temperature sensor;
3. a receiving circuit which includes the RX transducer, an amplifier with automatic gain control (AGC), an Analog-to-Digital Converter (ADC) and a FPGA for the signal processing.

3.3.1 Measurement cell

In the preliminary version, the measurement cell consists of a nylon tank, since this material can be easily fabricated into precision parts. Nylon, PEEK, PTFE and other engineering plastics also have the advantage of improved matching performances, with respect to traditional materials such stainless steel, since their acoustic impedance is between that of hard-piezoceramics and that of liquids.

The piezoceramics transducers (PZT-4E, 2.5 MHz centre frequency, by Medel Italiana or PZT PIC255, 2 MHz centre frequency, by Physik Instrumente (PI)) are pressed on the outer surface of the cell, with ultrasound gel in between which improves the mechanical contact. However the ultrasonic gel, composed by water, evaporates in few hours and, in a final setup, should

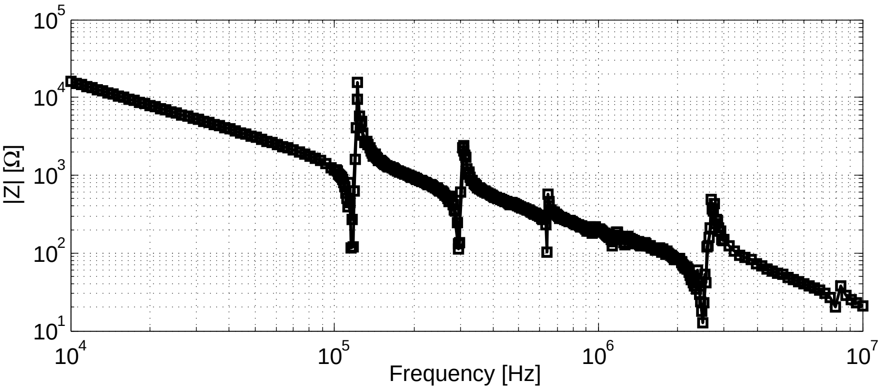

Figure 3.5: Impedance modulus of the piezoceramic transducer PZT-4E, 2.5 MHz centre frequency, by Medel Italiana.

be substituted by conductive epoxydic resins, with the advantage of fixing the transducers and providing electrical contact at the same time.

The contribution on the TOF of the tank walls (and of the matching layers) can be easily estimated and subtracted from the final result performing some preliminary calibration measurements.

Since temperature affects the ultrasonic velocity in liquids, and this dependence is known [40, 41], a temperature probe is inserted in the cell close to the transducers for obtaining more accurate estimates.

3.3.2 Transmitting circuit

The transmitting circuit includes a pulse generator which drives the ultrasonic transducer. The electrical impedance of the piezoelectric transducer is like that reported in Fig. 3.5, where the thickness mode vibration corresponds to the fourth resonance (approximatively at 2.56 MHz), and the maximum of transduction efficiency is obtained if the electrical stimulus is at the series resonance. Piezoceramic materials presents multiple resonances corresponding to different vibration modes: only one is the fundamental thickness mode which has to be excited for obtaining a longitudinal pressure wave in the liquid.

Since in TOF measurements a pulsed stimulus has to be used instead of a pure sine-wave, a preliminary analysis on the effect of the pulse shape was done.

In this phase, the applied transmitter setup was composed by an arbitrary waveform generator (Tabor Model 1072) connected to a high-speed buffer feeding the transmission ultrasound transducer. A high-speed digital-storage oscilloscope (Tektronix TDS3032, 300 MHz of bandwidth) simultaneously acquired the electrical signals at the transmitting and receiving transducers.

Three pulses with three different shapes have been applied to the transmitter:

1. a single sine pulse, with duration $t_S = 390\,\mathrm{ns}$ given by the period of a sinewave at $\sim$2.56 MHz;
2. a rectangular pulse with duration t_R and rising and falling times shorter than 30 ns;
3. a Gaussian pulse with a full width at half maximum (FWHM) t_G.

For all pulses a peak-to-peak amplitude of 2 V was imposed.

The peak-ot-peak output signal at the receiver was approximatively 190 mV for the single-period sine pulse, increasing for a sine pulse train up to $\sim$1.3 V when 10 sine-wave periods were used. However, a pulse train generator is more complex than Gaussian or rectangular pulse generators.

Gaussian and rectangular pulses should present a sufficient power spectral density in a narrow bandwidth close to the fourth resonance of Fig. 3.5. For the Gaussian pulse, the output signal reaches its maximum peak-to-peak value of $\sim$180 mV for $t_G = 165\,\mathrm{ns}$, which corresponds to a $-3\,\mathrm{dB}$ bandwidth $f_{-3dB} \sim 1.9\,\mathrm{MHz}$, on a good agreement with what was expected.

On the contrary, the behaviour of the rectangular pulse was little strange. The peak-to-peak output value varies, but not monotonically, as the pulse width shortens, as shown in Fig. 3.6(a). An explanation was found in the fact that both the rising and the falling edges of the rectangular pulse excite the mechanical vibration of the transducers and generate two waves which, reaching the receiver, can interfere, increasing or not the output signal depending on their relative phase. Such phase shift is a function of the rectangular pulse width. The system response to rising and falling, well-spaced, edges were measured for obtaining the two different waves, and so numerically estimating the interference effect by varying the phase shift, Fig. 3.6(b). The peak-to-peak values of that resulting waveform were compared with the measures obtained for different pulse widths showing a good agreement.

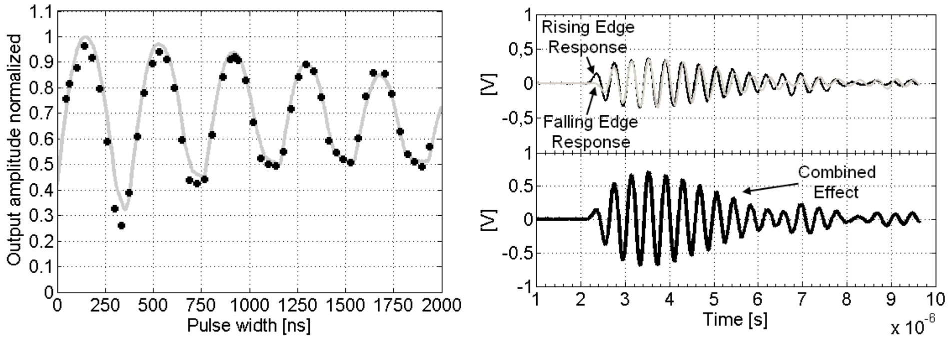

(a) *Simulation (line) and measurement results (markers) with rectangular pulse.*

(b) *Simulated interference.*

Figure 3.6: (a) Variation of the peak-to-peak output signal as a function of the width of the rectangular pulse on the transmitter. Markers refer to experimental results, line to simulations. (b) Single responses to the rising and falling edges of the transmitted pulse, and their combined effect.

Another relevant parameter is the edges' slope of the excitation signal. Faster fronts have wider bandwidth ensuring greater excitation of the piezoceramic transducer resonance. Some measurement results obtained with different edge times are reported in Fig. 3.7. It is evident that the wave edges have to be shorter than 50 ns for the effectiveness of the stimulus.

Therefore, a simple step signal can be used as excitation stimulus for obtaining a clear response on the receiving transducer. Moreover simpler and more reliable buffers and pulse generator circuits can be designed.

The transmission buffer has been reduced to a simple CMOS driver, the only constrains were on the rise, and the fall, time of the output and on the maximum driving amplitude. In Fig. 3.8 a simple representation of the transmission system is shown.

The electrical model of a piezoelectric transducer can be described as a capacitor in parallel to few RCL series circuits, one for each resonance. It is possible to extract each component of such equivalent model through an interpolation of experimental data, obtaining for the used transducer a parallel capacitor $C_p = 726\,\text{pF}$ and a series resistance for the interesting series branch

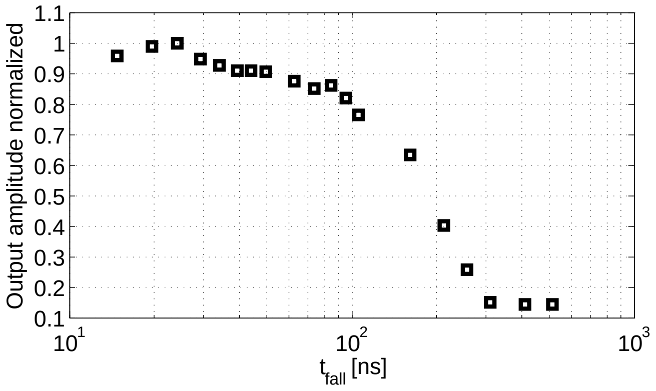

Figure 3.7: Measured peak-to-peak amplitude of the received signal for different slopes of the step signal used as stimulus.

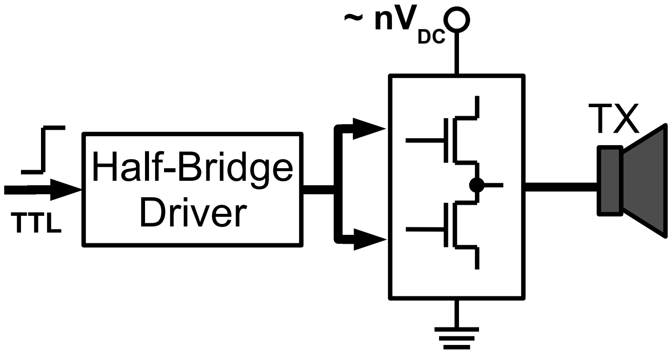

Figure 3.8: General outline of the transmitter.

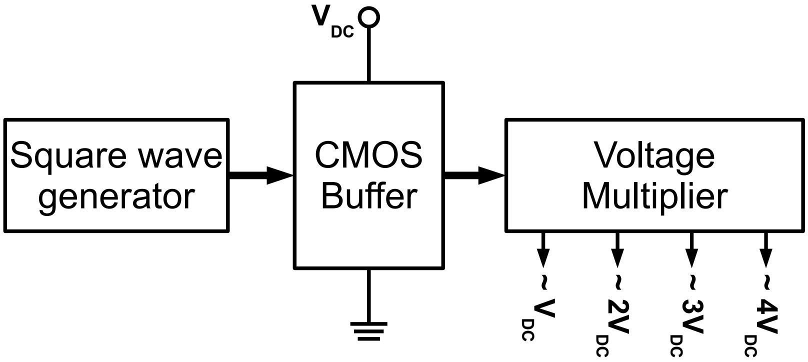

Figure 3.9: Block diagram of the voltage multiplier used for the power supply of the half bridge in the transmitter.

$R_s = 13\,\Omega$: the buffer must be able to drive these loads.

To this aim, the transducer has been connected to the central terminal of a half-bridge of dual n-MOS, able to drive up to 600 V of V_{DS} with about 15 ns of rise and fall time. This circuit, the STP6NK60Z, is normally used for high-current and high-speed switching designs, so it could be quite oversized for the application but adapted at this phase of the study because it is still not known the exact power needed in the transmission for obtaining the desired accuracy on the TOF measurement.

An additional driver circuit is necessary for achieving the correct driving potentials since the half-bridge is made of two n-MOS. The IRS21834 driver, with TTL inputs has been selected.

In addition, a voltage multiplier has been designed for obtaining, from a standard $V_{DC} = 24$ V supply, higher voltage values for supplying the half bridge. A Villard cascade voltage multiplier circuit was designed and four different outputs ($\sim V_{DC}$, $\sim 2V_{DC}$, $\sim 3V_{DC}$ and $\sim 4V_{DC}$) were obtained using a four stages architecture; the voltage drop on the diodes of the circuit limits the effective multiplied voltage to some volts below the expected value.

The multiplier should be powered with an alternate potential that has been obtained using a simple CMOS buffer/driver, the TC4432, able to drive loads up to 30 V, driven by a simple square wave generator. An overview of the whole multiplier circuit is reported in Fig. 3.9.

The half-bridge driver has a static absorbed current limited to the leakage of the mosfets only, but the peak current, during the switching time of the piezoceramic transducer, reaches about 150 mA with the power supply at 4×24 V. From the exponential behaviour of the current measured when the transducer capacitor is charged or discharged, it is possible to estimate a total amount of charge of about $Q_{sw} = 150\,\mathrm{nC}$. From this, forcing a 5% maximum of voltage drop during the switching, it is possible to obtain the minimum value for the capacitor C_m inside the multiplier:

$$C_m = \frac{Q_{sw}}{0.05 V_{tot}} = \frac{150\,\mathrm{nC}}{0.05 \cdot 96\,\mathrm{V}} \simeq 31\,\mathrm{nF}\,. \tag{3.12}$$

The value of these capacitors, together with the frequency of the chopped supply voltage, ensure that the outputs of the multiplier will be maintained on the correct values also in loaded condition. Experimentally, using 47 nF capacitors, a frequency of ∼40 kHz and a DC supply of 24 V, the output of the last stage remains at about 91 V with the piezoceramic connected as load. For comparison, 93 V were measured when no loads were connected to the multiplier outputs.

3.3.3 Receiving circuit

The strength of the received signal, as already written, is affected by several parameters of the material in which the ultrasound wave propagates. Such parameters can also change their values over the time so the amplitude could be different between subsequent measurements.

In order to limit this variability, a first-stage buffer amplifier with automatic gain control (AGC) has been inserted just after the transducer. The AD8367 has been used for that purpose since it integrates a variable gain amplifier and a square-law detector for the strength of the input signal. A regulated signal can be obtained by connecting the detector output to the gain input of the amplifier and by setting the amplifier so as to induce a lower gain for higher values of the detector output. Notice that the AGC could modify the signal shape because higher gains are expected for the first and the last cycles of the signal which are smaller. To preserve the actual waveform but, at the same time, to amplify the signal and obtain the same amplitude regardless of the propagation losses, a peak detector on the gain signal has been used. When the strength of the input signal reaches the peak value, the peak detector saves such potential and uses it as fixed gain. Therefore, the first

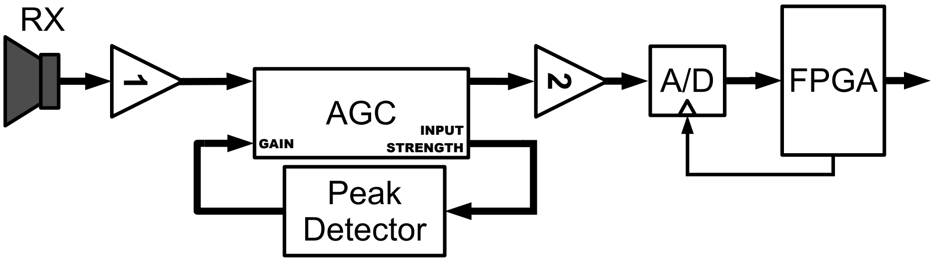

Figure 3.10: Block diagram of the receiver circuit.

received signal is used for setting the gain, the following ones will be correctly regulated.

Finally, a resistor has been placed in parallel to the hold capacitor of the peak detector for tracking the amplitude variations and consequently modifying the gain. The value of this resistor depends on the transmission rate: if too low resistances are used, the peak detector will not be able to hold its output up between successive received signals, on the contrary high resistor values will fix the output to the last peak detected for a long period, blocking the automatic regulation of the gain. In correct operation the hold capacitor should be continually and slowly discharged so that each received signal will take the gain back to the correct value. It is plain the trade off between the regulation accuracy and the response time to amplitude variations.

The regulated output of the AGC is then amplified for adjusting its fixed amplitude to the input range of an ADC. As it will be explained below, the requirements for the A/D converter are 12-bit resolution and 20 MSamples/s. Therefore, an ADS805 with unipolar power supply and single-ended input connection has been chosen.

The ADC is connected to an external FPGA (Xilinx Spartan-3E) which provides the sample clock and saves the converted values for the post processing. The overall block diagram of the receiver is shown in Fig. 3.10.

3.4 Digital Signal Processing

During alcoholic fermentation, ultrasound velocity can change from ∼1400 m/s to ∼1700 m/s, and a resolution of 0.05 m/s is often required.

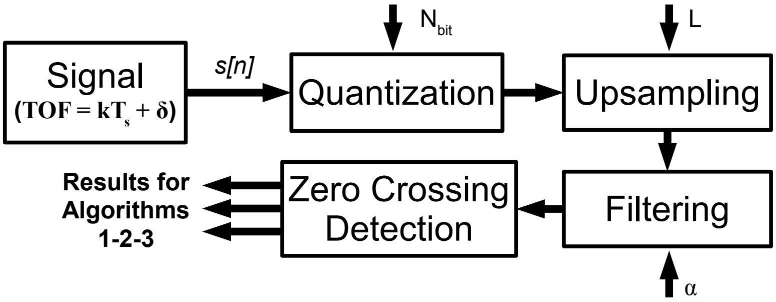

Figure 3.11: Block diagram of the signal processing sequence.

Therefore, for a distance $d = 3\,\mathrm{cm}$ between transmitter and receiver a resolution of, approximatively:

$$u(t) \simeq \frac{u(v)}{v^2}\, d = \frac{5 \cdot 10^{-2}}{(1.7 \cdot 10^3)^2}\, 3 \cdot 10^{-2} \simeq 500\,\mathrm{ps}\,, \tag{3.13}$$

has been assumed. It is obvious that this requirement cannot be reached merely increasing the sampling frequency of the ADC, so that the FPGA should estimate the zero-crossing times by means of a signal processing procedure. This procedure has been firstly developed in MATLAB and then transferred on the FPGA.

For the MATLAB simulations, the received signal was modelled as:

$$s(t) := \begin{cases} a \cdot (t - t_0)^2 \cdot e^{-b \cdot (t - t_0)} \cdot sin(2\pi f_p (t - t_0)), & \text{for } t > t_0, \\ 0, & \text{for } t < t_0, \end{cases} \tag{3.14}$$

where a and b are numerical coefficients, f_p is the resonance frequency of the piezoelectric transducer and $t_0 = kT_s + \delta$ is the TOF. The sampling starts, for each repetition, after a different $\delta \in [0 \quad T_s]$ to reproduce the variability of the arrival time of the wave. The output signal is therefore quantized, according to the number of bits used, upsampled adding $L - 1$ zero samples between the real samples, filtered and finally elaborated for estimating the zero-crossing points.

A schematic of the signal processing sequence is given in Fig. 3.11. Since for a pulse train under low sampling rate it is not so obvious that the required resolution could be obtained from the raw data, these are upsampled and then filtered by an interpolation, linear-phase, FIR filter. Finally the zero-crossing times are extracted from the resampled data. In Fig. 3.11, some processing steps and parameters are highlighted:

- the upsampling rate (interpolation factor L);
- the bandwidth of the interpolation filter (α, $1 =$ Nyquist frequency);
- the zero-crossing detection algorithm;
- the number of bits of the ADC (N_{bit});
- the sample frequency ($f_s = \frac{1}{T_s}$).

Now several series of results, obtained varying one or more parameters and repeating the simulation 500 times, will be shown. For each plot will be reported the standard deviation of the error between the estimation and the effective zero position, and, moreover, their behaviour for different upsampling rates. For clarity, in the reported results only the first zero evaluation has been shown even if the simulations have been done considering the firsts 15 zero-crossings. Others zeros will be taken into account using the final configuration only.

3.4.1 Zero-crossing estimation

Once the acquired signal is resampled, the algorithm looks for the sign changes and estimates the zero-crossing times as:

1. the average between the times corresponding to samples before and after the sign change;
2. the linear interpolation between these same samples;
3. an interpolation on a 3rd order polynomial between two samples before and two after the sign change.

Let consider, for instance, the case $f_s = 20\,\mathrm{MHz}$, $\alpha = 0.5$, and $N_{bit} = 10$ reported in Fig 3.12. The simple average provides an unsatisfactory repeatability, even for high-interpolation factors, and both the other two methods,

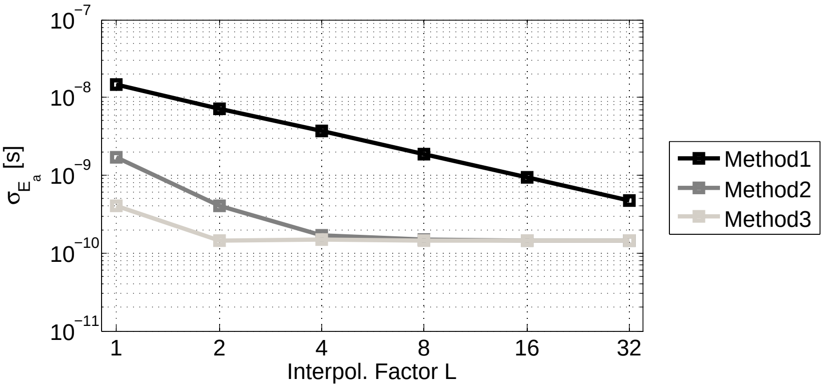

Figure 3.12: Standard deviation of the time estimation for different methods for the zero-crossing detection. Fixed parameters: $\alpha = 0.5$, $f_s = 20\,\text{MHz}$, $N_{bit} = 10$.

for interpolation factors $L \geq 8$, allow obtaining, in a noiseless environment, a repeatability better than 150 ps, basically bounded by the low resolution of the ADC. Therefore, since the use of a 3rd order polynomial does not improve the accuracy, hereafter only the zero-detection based on the linear interpolation will be accounted for.

3.4.2 Sampling frequency effect

The sampling frequency, together with the converter resolution, is probably the parameter which mainly influences the complexity of the design rules. However, it is evident that an increase of the sampling frequency might also improve the measurement accuracy.

Fig. 3.13 shows that, for $\alpha = 0.5$ and $N_{bit} = 10$, this is true only for interpolation factors $L < 8$, since the advantage of increasing the sampling frequency is defeated by the quantization noise for $L \geq 8$ and $f_s \geq 15\,\text{MHz}$.

3.4.3 Influence of the interpolation-filter bandwidth

A linear-phase FIR filter has been used as interpolation filter after the upsampling, limiting the elaboration to the nearest six, not-null samples in order to reduce the complexity. With such filter it is possible to limit the bandwidth

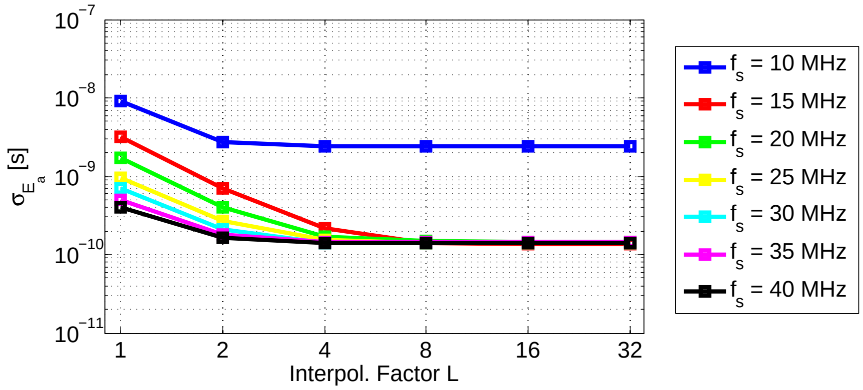

Figure 3.13: Expected measurement standard deviations for different sampling frequencies, with $\alpha = 0.5$ and $N_{bit} = 10$. Linear interpolation is the method chosen for the zero-crossing detection.

of the interpolated signal modifying the α parameter. The Nyquist frequency $f_N = 1/(2T_s)$ corresponds to $\alpha = 1$. With $\alpha = 0.5$ the bandwidth reduces to $f_N/2$, and so on.

Fig. 3.14(a) shows the simulation results corresponding to $f_s = 15\,\mathrm{MHz}$ and $N_{bit} = 10$. The standard deviation presents a minimum for $\alpha = 0.5$. Since $f_s = 15\,\mathrm{MHz}$ is a lower bound for the sampling frequency, it is interesting to compare these data with those at an higher frequency, $f_s = 20\,\mathrm{MHz}$ of Fig. 3.14(b). For sampling frequencies $f_s \geq 20\,\mathrm{MHz}$, the filter bandwidth can be reduced without any appreciable detriment to the standard deviation σ_{E_a}, but with an obvious advantage with respect to the voltage noise which foul the received signal.

3.4.4 Influence of the number of bit

The last design parameter to be chosen is the resolution of the A/D converter. For $\alpha = 0.5$, $f_s = 15\,\mathrm{MHz}$, and interpolation factor $L \geq 8$, the standard deviation σ_{E_a} decreases from an unsatisfactory value of ~550 ps for a 8-bit ADC to ~120 ps (~50 ps) for a 10-bit (12-bit, respectively) ADC, as can be observed in Fig. 3.15.

Therefore, a 12 bit ADC with sampling frequency of 20 MHz, and an interpolation factor of $L = 8$, have been chosen.

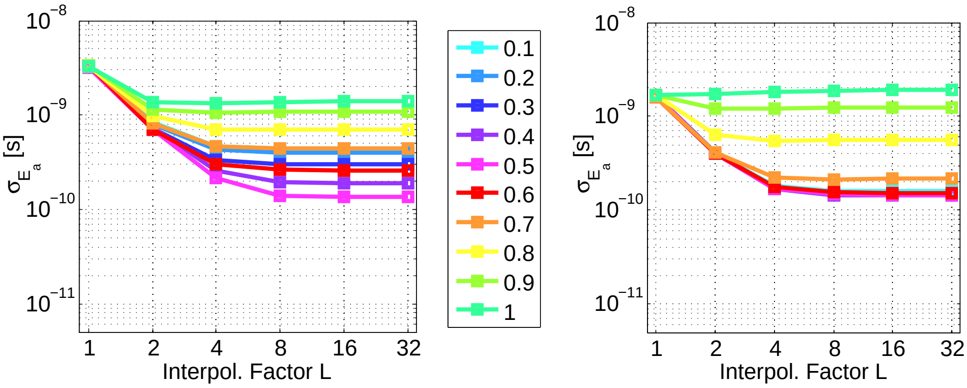

(a) $f_s = 15\,\mathrm{MHz}$.

(b) $f_s = 20\,\mathrm{MHz}$.

Figure 3.14: Expected measurement standard deviations for different interpolation-filter bandwidths and for $N_{bit} = 10$. Linear interpolation is the method chosen for the zero-crossing detection.

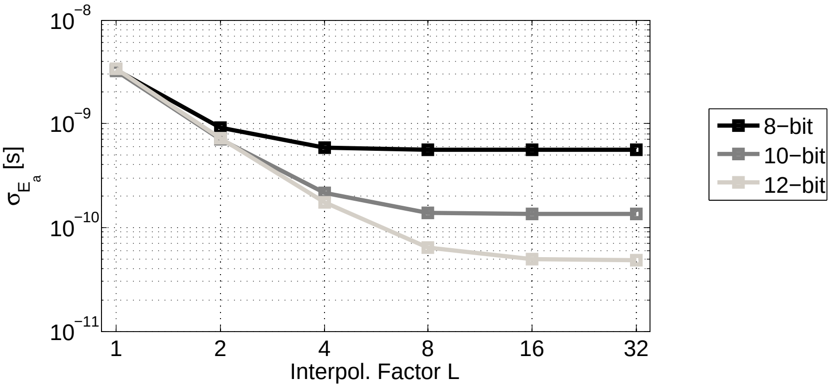

Figure 3.15: Standard deviation of the time estimation for different resolutions. Fixed parameters: $\alpha = 0.5$, $f_s = 15\,\mathrm{MHz}$, and a linear interpolation for the zero-crossing detection.

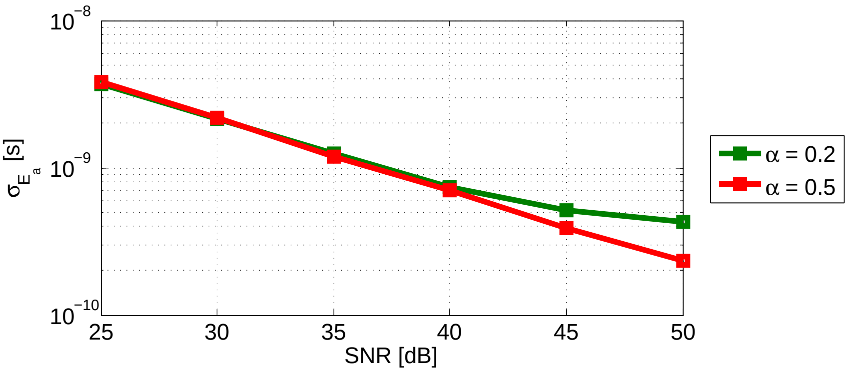

Figure 3.16: Standard deviation of the time estimation for different SNR. Fixed parameters: $f_s = 15\,\text{MHz}$, $N_{bit} = 12$, and a linear interpolation for the zero-crossing detection.

3.4.5 Noise Effect

Finally, Gaussian noise was added to the received signal just after the sampling, before the quantization. This kind of simulation can be useful to verify the performances in more realistic conditions because, for instance, a merely seeming advantage might result from an increasing number of bits.

Fig. 3.16 shows the standard deviation for $f_s = 15\,\text{MHz}$, $N_{bit} = 12$, and $L = 8$ as a function of the Signal-to-Noise ratio for different values of α. It can be noticed that the uncertainty level directly depends on the SNR ratio and α does not influence the results for $f_s = 15\,\text{MHz}$, especially for high noise levels.

3.4.6 Zeros-crossing times following the first ones

Once found the best configuration parameters that can permit to achieve the requested specifications, it is possible to verify if the detection of the zero-crossing instants following to the first one, could improve the performances of the system.

Simulations has been repeated for the other zero-crossing points, with $\alpha = 0.5$, $f_s = 15\,\text{MHz}$, and $N_{bit} = 12$. Fig. 3.17(a) reports the achievable performances, in noise absence, for the first seven zero-crossing times: it is apparent that the standard deviation decreases up to the detection of the fifth zero, and then increases again for the next ones. The reason of such an effect can be found in the amplitude of the received signal: when the amplitude of the envelope reaches its maximum, the slope of the signal at the nearest zero-crossing time is the highest, reducing the jitter uncertainty.

Repeating the simulation in presence of noise and focusing on the fifth zero-crossing time, the results shown in Fig. 3.17(b) are obtained. Comparing the results with the corresponding ones found for the first zero-crossing time, it can be seen that the same standard deviation of about 2×10^{-10} s, obtained evaluating the first zero with $SNR = 50\,\mathrm{dB}$, can be achieved using the fifth zero with a SNR 10 dB smaller.

3.5 Conclusions

From the simulation results it has been gathered that lower uncertainty levels can be obtained on the zero-crossing times following the first one. For the TOF estimation, these values can be singularly used after an initial calibration phase, necessary for compensating the propagation delay through the wall of the measurement cell and the matching layers. This allows obtaining several TOF values, which could be finally combined for an improved measure with a weighted mean based on the *a-priori* estimated uncertainty levels.

The transmission system, with the receiver and the transmitter boards, has been implemented and characterized in its singular components, but experimental results of the complete system are not currently available.

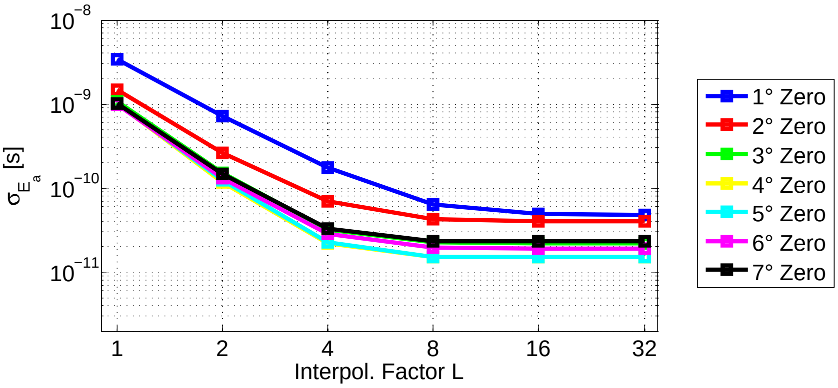

(a) *Zeros comparison.*

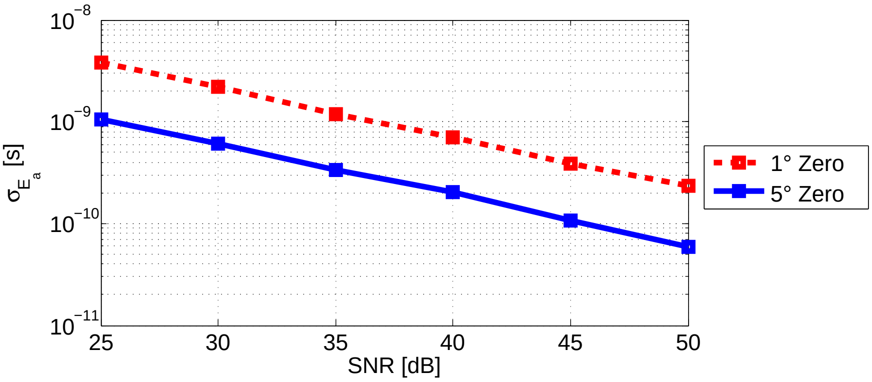

(b) *Results for the 5° zero detection, in presence of noise, compared with the 1° zero detection.*

Figure 3.17: Standard deviation of the time estimation for different zeros. Fixed parameters: $\alpha = 0.5$, $f_s = 15\,\mathrm{MHz}$, $N_{bit} = 12$, and a linear interpolation for the zero-crossing detection.

CHAPTER 4

Fringe activity: Pulsed periodic flow rate monitoring using a hot-film anemometer [42]

4.1 Introduction to the problem

The efficiency of industrial production processes is a critical element that directly impacts on the quality and on the cost of the final products. To achieve high efficiency levels, production lines are monitored by devices which detect, and possibly prevent, problems during the process.

In the dispensing of adhesive materials, dosing errors are particularly related to the physical properties of the glue and to the mechanical characteristics of the dispensing device: adhesive materials are characterized by a temperature dependent viscosity and a certain compressibility. Fluctuations in the operating temperature can influence the viscosity of the material and changes in the applied pressure can result in a dosing error: in case of overdose, contamination and fouling of the production components can occur, while an inadequate dose can cause a reduction in the tightness and durability of the adhesive materials.

The proposed flow monitoring system has been designed for a worldwide leader factory in order to detect dosing errors is a dispensing process and it has been developed using the anemometry technique.

In fact, hot-wire anemometers are commonly used in flow monitoring systems. Essentially, hot-wire anemometry is an indirect measuring technique based on the heat transfer from a heater sensing element which is cooled by an unsteady compressible flow.

The typical measurement circuit is based on a thin wire with a well-know temperature dependent resistance value. Two different modes of operation of the hot-wire are possible, the Constant Voltage Anemometer (CVA) and the Constant Temperature Anemometer (CTA). With regard to the CTA system, the conditioning circuit heats that wire and measures the power absorbed in order to hold the temperature fixed at some degrees over that of the liquid. Such power value will be directly proportional to the flow speed in which the wire has been dipped in.

In this particular application, the flow shows a pulsed periodic behaviour that does not fall in the normal hypothesis used in the design process of the conditioning circuit. For this reason a different approach has been thought.

4.2 The designed system

A hot-film anemometer has been preferred compared to an hot-wire one because of its strength and reliability when used for flow monitoring applications in industrial environments [43]. Hot-wire sensors could have greater sensitivity and faster responses, due to their extremely limited dimensions, but they will be quite breakable. The implemented calorimetric sensor FS5L (manufactured by INNOVATIVE SENSOR TECHNOLOGY) consists of two platinum resistance temperature detectors, realized with a thin film deposited onto a 2.4 mm x 7 mm x 0.15 mm ceramic substrate of aluminium oxide. Using both the resistances, as explained in [44], allows to have a direct compensation of possible temperature variations of the liquid during the measurement. The sensor presents a nominal response time ($t_{63\%}$) in distilled water, at room temperature, of less than 100 ms while the mechanical dispenser, used in the production process for the flow control, is characterized by a flow rate of adhesive material ranging from about 0.1 m/s to 15 m/s with a configurable dispensing time ranging from 0.5 s to 5 s.

It is apparent that the sensor characteristics do not grant adequate dynamic performances when short dispensing times are used in the dosing process, so a direct tracking of the flow speed is not possible. Some compensation techniques have been presented in [45, 46, 47, 48] for different kinds of anemometers. Hot-wire anemometry is suggested in [49] for high speed pulsating velocity measurements while in [50] the application of such devices seems to be limited only to small-amplitude fluctuations without flow reversal. Moreover, new procedures are suggested to properly correct the non linearities, due to the thermal inertia of the wire for large velocity fluctuations, based on a CVA (Constant Voltage Anemometer) in [51].

A CTA (Constant Temperature Anemometer) configuration has been preferred to avoid long thermal transients, however it is difficult to implement a complete compensation for wide flow rate ranges because of thermal parameters variation for different flow speed conditions. Therefore a different approach has been chosen: the uncompensated signal will be directly used to monitor the dosing operation. This approach can be useful also when the sensor parameters are unknown or when different kinds of sensors are used with the same conditioning circuit, ensuring greater flexibility.

In order to correctly check the dosing process, the monitoring circuit is connected to a system controller, a user programmed device which defines the operating parameters of the process (the dosing period T_{dose}, the dosing time t_{dose}, and the flow pressure of the glue) controlling the mechanical dispenser, see Fig. 4.1. The system controller provides the flow monitoring system with a *trigger* signal, that is a periodic signal characterized by a duty cycle $D = t_{dose}/T_{dose}$, which traces out the effective mechanical dispensing of adhesive material through the valve which defines the flow velocity. During each dosing period the monitoring device sends the *monitor* signal to the system controller. This signal is taken from the output of the CTA and provides information about the quality of the dispensing process. Finally, it is compared with previously memorized samples, used as a reference by the system controller, in order to detect any differences.

Several tests were performed by measuring the response of the device with liquids characterized by different thermal conductivities to properly check the operating boundaries of the monitoring system. Such measurements were done on distilled water and ethanol, these liquids present a viscosity similar to the one of the adhesive materials, and thermal conductivities which cover the same range of the operating parameters characterising the adhesive materials used in the dispensing system. Viscosity and thermal conductivity of these two liquids are reported in Table 4.1.

In Fig. 4.2 the output of the CTA circuit is reported for the two liquids and different dosing rates. The provided signals present different amplitudes and remarkable offsets highlighting different possible conditions. The offset can be ascribed to the duty cycle of the dosing process and to the dynamic behaviour

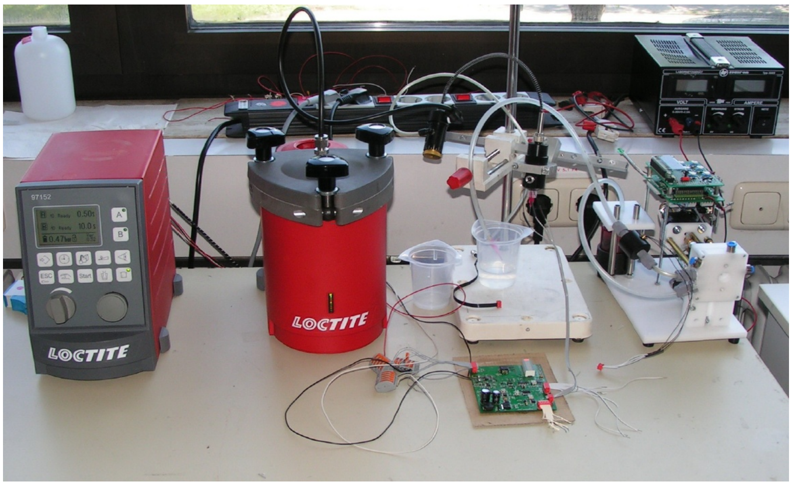

Figure 4.1: Test setup of the system. On the left the system controller, in the centre the mechanical dispenser with the designed flow monitoring board, and on the right the velocity calibrator.

Table 4.1: Distilled water and ethanol parameters.

	Viscosity (η)	Thermal conductivity (k)
Distilled Water	0.894 mPa	0.58 $\mathrm{W/(m \cdot K)}$
Ethanol	1.074 mPa	0.17 $\mathrm{W/(m \cdot K)}$

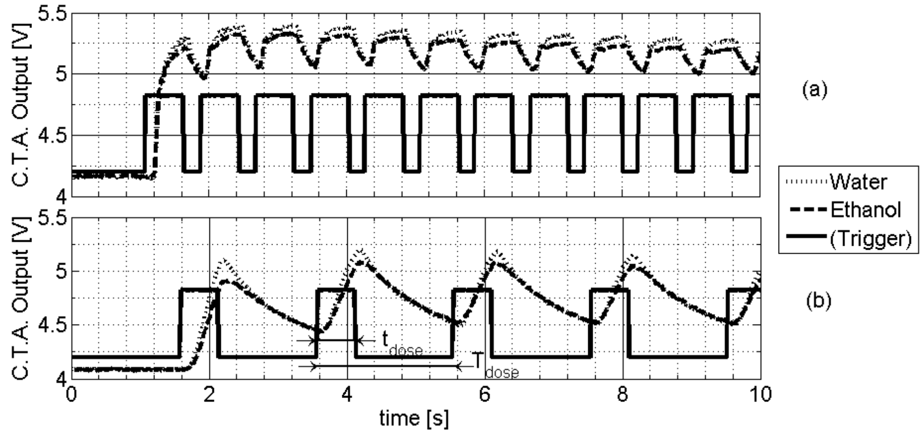

Figure 4.2: Output of the CTA circuit for different liquids and different rates: in (a) the dosing period T_{dose} is 0.8 s while in (b) is 2 s. Dispensing time t_{dose} is fixed to 0.5 s for both. Trigger signal shows the reference signal provided by the dosing machine and has been scaled down in amplitude for make easier the comparison.

of the sensor during the thermal transients, related to the sensor thermal capacitance. The amplitude, instead, is affected by the duty cycle again and by distinct thermal conductivities of the two fluids: the thermal conductivity of distilled water, k_{H_2O}, greater than that of the ethanol, $k_{C_2H_6O}$, causes more thermal energy to be transferred from the calorimetric sensor to the liquid, therefore resulting in a greater amplitude of the water's output signal.

It is important to notice in Fig. 4.2 that, during the initial dosing process, the two signals, characterized by different duty cycles, are slightly different. At the beginning, the device starts always from the same initial conditions and therefore the resulting signals should be equal until the end of the first dose, regardless of t_{dose} or T_{dose}; afterwards the thermal transients will modify the output signal of the anemometer. Those different waveforms are due to the valve of the mechanical dispenser that does not allow reproducing the periodic flow with the same operating parameters among different measurements. Since such experimental inaccuracy has proved to be useful to verify the reliability of the system in a more realistic scenario, no efforts have been made to correct such behaviour.

In Fig. 4.3 the functional structure of the flow monitoring system with

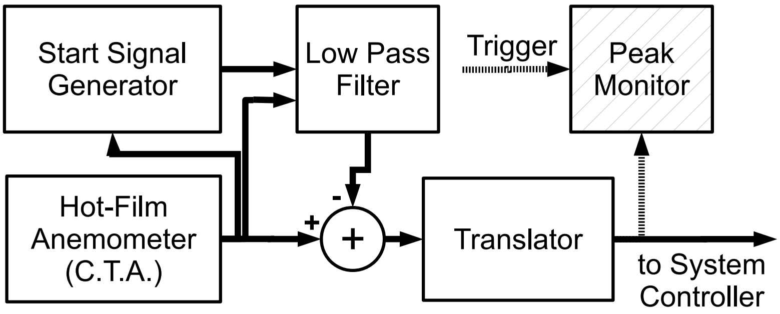

Figure 4.3: Block diagram of the designed conditioning circuit.

its main elements is shown. The CTA provides the signal, derived from the measured flow rate, to the correction circuit; this circuit, realized by a second order Butterworth low pass filter and an adder, removes the DC component of the input signal by subtracting its average value. This configuration has been preferred to a simple high-pass filter in order to have a better response with long T_{dose} and permit easier future modifications if necessary. The resulting output of the correction circuit is not affected by drift errors related to the physical limitations of the calorimetric sensor and, after an electrical matching performed by the translator block, the signal is sent to the system controller ensuring a clear indication of the flow behaviour, also in the case of a dosing periods $T_{dose} \leq 1\,\mathrm{s}$ and duty cycles $D \geq 0.5$.

The CTA circuit is based on a Wheatstone bridge and a high gain instrumentation amplifier with an emitter follower current buffer [52]. In the balance condition the differential temperature $\Delta T = T_V - T_a$ between the flowing fluid and the sensor is approximately 5 °C. Although in normal applications the suggested value of ΔT is higher, considering how the characteristics of adhesive materials are temperature dependent, a lower differential temperature has been chosen in order to avoid the presence of a local hot point in the dispensing tube.

The period of the signal obtained from the CTA, due to the dispensing parameters and so in the order of seconds, requires poles at extremely low frequencies for the low-pass filter of the correction circuit. In particular, if a maximum dosing period equals to $T_{dose_{max}} = 5\,\mathrm{s}$ is assumed, the filter should be designed to have a cut-off frequency $f_c = 0.1\,\mathrm{Hz}$ at the expense of a very long settling time that hampers a correct handling of the first doses after a stop event. For this reason, a Start Signal Generator (SSG) circuit has been designed in order to generate a digital signal which defines the start of the dosing process, not only at the beginning of the process but also after a temporary stop of the mechanical dispenser. At the beginning of the monitoring process, after the start up of the device and with null flow rate, the hot-film anemometer reaches quickly the equilibrium and the output idle level. During this time a voltage comparator in the SSG circuit compares the anemometer output with a threshold level, greater than the balance condition. When the dispensing machine is activated, during the first dosing period, the sensor, reacting to the flowing fluid, causes the output voltage of the anemometer to grow above the threshold: the comparator senses such variation and enables the SSG output. Such impulse controls an analog switch in the correction circuit, that temporary converts the low-pass filter in a simple follower circuit bringing the filter output to a level closer to the final one. In this way, as it is possible to see in Fig. 4.4, during the first dosing period the output signal of the correction circuit closely follows the anemometer output overcoming the limit of the low-pass filter. It should be noticed that the impulse length is a critical parameter because, as reported in Fig. 4.4, too high values help a fast achievement of the correct average value, but the first dose could be not detected. Finally, the Translator block amplifies and shifts the output signal of the correction circuit to more suitable levels in order to match the electrical specifications of the system controller, Fig. 4.5.

As indicated in Fig. 4.3, the flow monitoring system presents an experimental device, the Peak Monitor (PM), implemented in order to replace, or only assist, the comparison made by the system controller.

The PM circuit simply provides the peak value of the output of the correction circuit during each dosing period. It is based on a classic peak detector circuit, but its design has been enhanced by the implementation of an analog switch, connected to the hold capacitor, driven by the trigger signal of the system controller. During the dosing time, the switch connects the capacitor to ground so the output of the PM is fixed to zero. When the dosing time is over, the switch opens and the circuit starts to work as a normal peak detec-

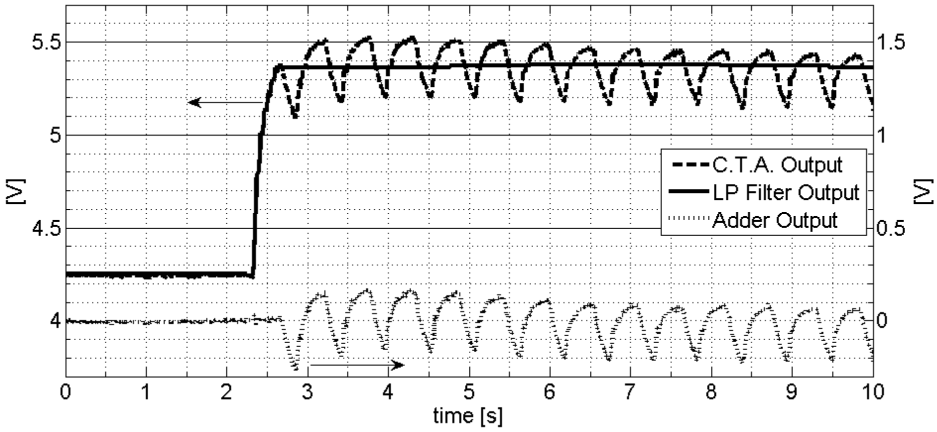

Figure 4.4: CTA signal, filtered signal and conditioning circuit output are shown. In this measurement a too long impulse for the SSG circuit has been chosen and, as a consequence, the first dose is lost by the monitoring circuit.

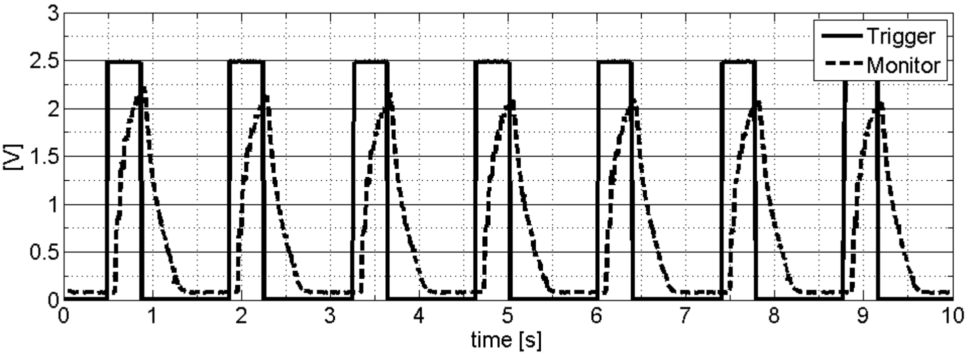

Figure 4.5: Trigger signal from the dosing system and final monitor signal provided to the system controller.

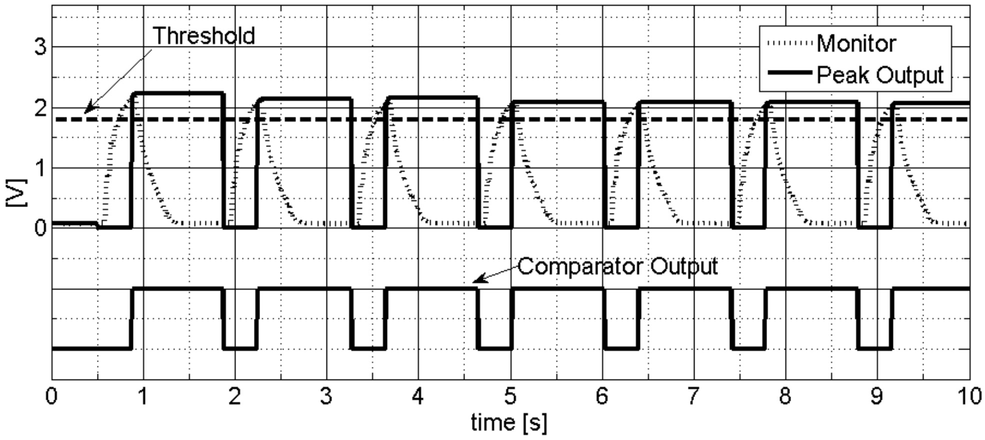

Figure 4.6: Simulation of the proposed alternative circuit for simplify the comparison made by the system controller to a simple threshold crossing.

tor saving the peak value of the CTA output. As reported in the simulation of Fig. 4.6, in which the measured *monitor* signal has been used, the monitor output has always a short delay respect the trigger signal due to the thermal inertia so, when the PM is enabled, the highest value of the *monitor* signal is saved. This level can be finally used for a simple comparison with another fixed threshold for verifying the dosing of a minimum adhesive quantity.

Performance tests have been carried out on the flow monitoring device showing a good reliability of the system in a wide range of experimental cases, characterized by different operating parameters of the dispensed fluid and time constraints of the dosing process. The reliability of the flow monitoring system has been achieved by the implementation of the correction circuit necessary to overcome the physical limitations of the measuring device, and designed to eliminate time dependent errors of the measured signal without affecting its integrity. In all the laboratory tests performed, the dispensing of non adhesive material has been correctly monitored and mechanical dispensing problems have been detected guaranteeing a high efficiency of the production process.

APPENDIX A

LCRcontroller Overview

LCRcontroller is the name of the application, MATLAB based, that allows to perform impedance measurements controlling at the same time the impedance meter, the switch unit and the temperature meter using the test bench reported in Fig. 1.12.

This program has been designed to allow the use of one of the two impedance meters available in our laboratories setting up the customized graphical interface at the connection. Others instruments can also be easily added thanks to the modular architecture of the program.

The initial screen is shown in Fig. A.1 and a list of the main features is reported:

- auto-detection of the *BoardIndex* of the USB/GPIB adapter;
- complete configuration of the measurement parameters (frequency, amplitude, bias, type of source, integration time, correction);
- selection of the results format;
- manual or automatic (by instrument or by application) range selection;
- automatic sweep for amplitude, bias and frequency with linear and logarithmic steps; nested sweeps are also possible;
- logging of the flowing current and the measured voltage;

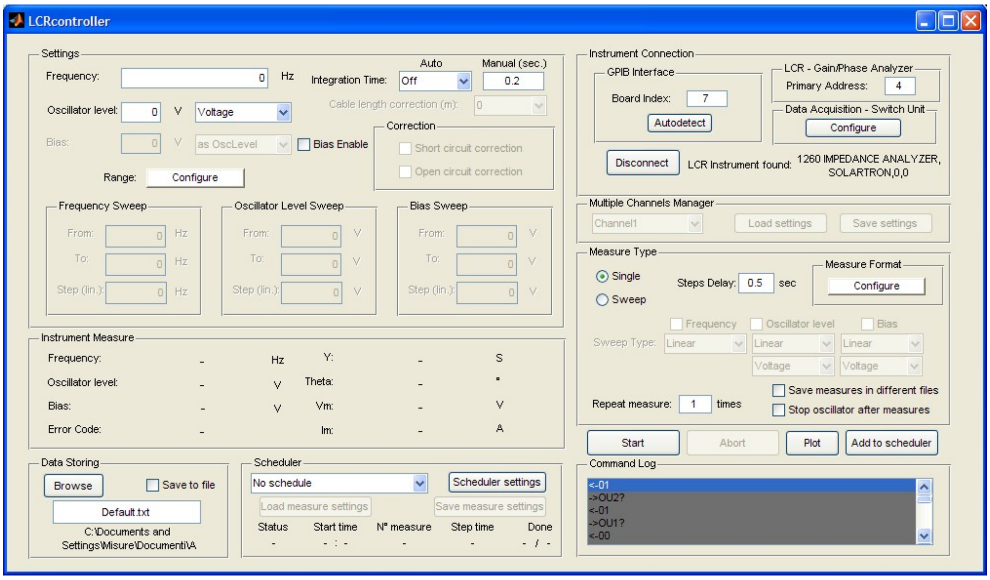

Frequency: 0 Hz
Integration Time: Auto: Off; Manual (sec.): 0.2
Oscillator level: 0 V Voltage
Cable length correction (m): 0
Bias: 0 V as OscLevel
☐ Bias Enable
☐ Short circuit correction
☐ Open circuit correction

Frequency Sweep — From: 0 Hz; To: 0 Hz; Step (lin.): 0 Hz
Oscillator Level Sweep — From: 0 V; To: 0 V; Step (lin.): 0 V
Bias Sweep — From: 0 V; To: 0 V; Step (lin.): 0 V

Frequency: - Hz
Oscillator level: - V
Bias: - V
Error Code: -
Y: - S
Theta: - °
Vm: - V
Im: - A

☐ Save to file
Default.txt
C:\Documents and Settings\Misure\Documenti\A

No schedule

Status	Start time	N° measure	Step time	Done
-	- : -	-	-	- / -

Board Index: 7
Primary Address: 4
LCR Instrument found: 1260 IMPEDANCE ANALYZER, SOLARTRON,0,0
Channel1

● Single
○ Sweep
Steps Delay: 0.5 sec
☐ Frequency ☐ Oscillator level ☐ Bias
Sweep Type: Linear Linear Linear
Voltage Voltage
Repeat measure: 1 times
☐ Save measures in different files
☐ Stop oscillator after measures

```
<-01
->OU2?
<-01
->OU1?
<-00
```

Figure A.1: Main screen of the LCRcontroller.

- concurrent measurements on up to 5 temperature sensors;
- automated measurements on up to 3 impedance sensors using the switch unit;
- it is possible to use both the Agilent 34970A Data Acquisition Switch Unit (GPIB) than the designed MuxBoard (RS-232) as a switch unit;
- scheduling of the measurements with configurable start and step times.

The application has been continuously improved for adding new functions and correcting possible faults. Two interesting issues, occurred in some particular conditions, were caused by the behaviour of the SOLARTRON 1260 impedance meter. Both of the issues are connected with the use of the automatic range selection.

The first odd behaviour occurs when the 6 µA range is selected for the current input. Sometimes during a measurement the instrument reports an overflow error even if the selected range is the correct one for the amount of

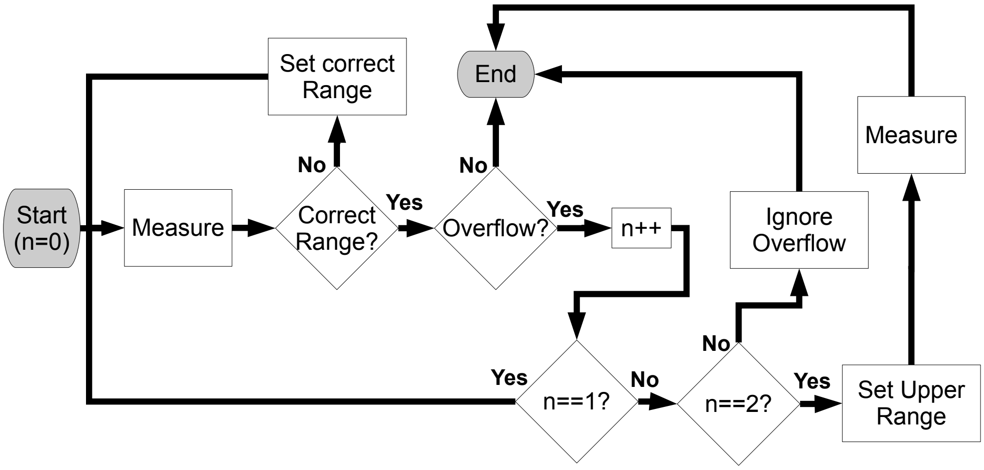

Figure A.2: Flowchart of the automatic range selection feature with the implemented solution for manage the unjustified overflow indication.

the flowing, and measured, current. When that happens, usually it is sufficient to repeat the measurement, with the same range, for obtaining a result without reported errors, but in few cases it is actually necessary to switch on upper ranges.

In Fig. A.2 the corresponding flow chart of the implemented solution is shown. As it is possible to see, when the correct ranges have been reached, depending on the measured voltage and current, if an overflow error occurs the measure is repeated one time more; if the overflow persists in the repetition, the range is increased and the measure is repeated for the last time and saved regardless any new overflow errors. This technique has been chosen for having a correct measure with the more suitable range, but at the same time for allowing a larger range if the overflow message is confirmed for two consecutive times.

The second issue regards the correct range to select in the measurements. When the voltage or the current value is slightly higher than the upper limit of a range, the application automatically repeats the measurement selecting the upper range; the results of this new measurement could now return in the lower range so the system resets the range to the lower value and repeats the measurement again. This last measurement could result again over the selected range and so on forever. The common solution to such a problem is

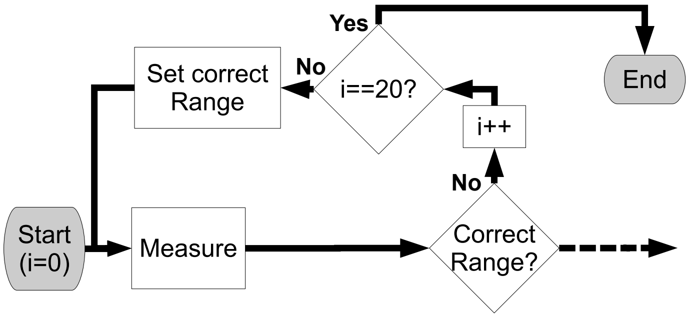

Figure A.3: Flowchart of the added system for limit the autorange selection iterations.

an hysteresis for the threshold selection but the wideness of such hysteresis is subjected to a trade off: when large gaps are used the best range available could not to be set for some measurements, on the contrary tight gaps could be still subjected by the initial problem.

The used solution implements a modification of the flowchart seen above in Fig. A.2. Instead of using hysteresis, a limit for the number on the range changes is imposed. The first part of the modified flowchart is reported in Fig. A.3. In this conditions, using an even number of allowed iterations can leads to two different cases:

1. if the initial range could be the correct one and the application starts to bounce with a range next to this, the loop will exit leaving the range next to the initial one for the measure;
2. if the initial range was wrong, in the first iteration the correct one will be set; if the bouncing with a range next to this new one starts at this point, it will be interrupted leaving as final range the first set.

In the first case the application tends to follow an increasing or decreasing of the measured impedance moving toward the next range. On the contrary, if a new range has been set with respect to the last measure, the rule is to remain in this new one.

Bibliography

[1] *Understanding Electrochemical Cells*, Solartron Instrument Technical Report 17 (1997).

[2] Prof. Spinelli Paolo, *Elettrochimica Applicata*, Academic course of Politecnico di Torino (2001).

[3] M. E. Orazem and B. Tribollet, *Electrochemical Impedance Spectroscopy*, Wiley (2008).

[4] L. Yang, and R. Bashir, *Electrical/electrochemical impedance for rapid detection of foodborne pathogenic bacteria*, Biotechnol. Adv. 26 (2008) 135-150.

[5] M. Varshney, and Y. Li, *Interdigitated array microelectrodes based impedance biosensors for detection of bacterial cells*, Biosens. Bioelectron. 24 (2009) 2951-2960.

[6] L. Yang, Y. Li, C. L. Griffis, and M. G. Johnson, *Interdigitated microelectrode (IME) impedance sensor for the detection of viable Salmonella typhimurium*, Biosens. Bioelectron. 19 (2004) 1139-1147.

[7] M. Jönsson, K. Welch, S. Hamp, and M. Strømme, *Bacteria Counting with Impedance Spectroscopy in a Micro Probe Station*, J. Phys. Chem. B 110 (2006), 10165-10169.

[8] R. Ehret, W. Baumann, M. Brischwein, A. Schwinde, K. Stegbauer, and B. Wolf, *Monitoring of cellular behaviour by impedance measurements on interdigitated electrode structures*, Biosens. Bioelectron. 12 (1997) 29-41.

[9] S. M. Radke, and E. C. Alocilja, *Design and Fabrication of a Microimpedance Biosensor for Bacterial Detection*, IEEE Sensors J. 4 (2004) 434-440.

[10] J.G. Guan, Y.Q. MIAO, and Q.J. Zhang, *Impedimetric Biosensors*, J. Biosci. Bioeng. 97 (2004) 219-226.

[11] O. Laczka, E. Baldrich, F.X. Muñoz, and F.J. del Campo, *Detection of Escherichia coli and Salmonella typhimurium using interdigitated microelectrode capacitive immunosensors: the importance of transducer geometry*, Anal. Chem. 80 (2008) 7239-7247.

[12] A. Sánchez, D. Sierra, C. Luengo, J. C. Corrales, C. de la Fe, C. T. Morales, A. Contreras, and C. Gonzalo, *Evaluation of the MilkoScan FT 6000 Milk Analyzer for Determining the Freezing Point of Goat's Milk Under Different Analytical Conditions*, J. Dairy Sci. 90 (2007) 3153-3161.

[13] M.F. Mabrook, and M.C. Petty, *Effect of composition on the electrical conductance of milk*, J. Food Eng. 60 (2003) 321-325.

[14] M.F. Mabrook, and M.C. Petty, *Application of electrical admittance measurements to the quality control of milk*, Sens. Actuators, B 84 (2002) 136-141.

[15] M.F. Mabrook, and M.C. Petty, *A novel technique for the detection of added water to full fat milk using single frequency admittance measurements*, Sens. Actuators, B 96 (2003) 215-218.

[16] M.F. Mabrook, A.M. Darbyshire, and M.C. Petty, *Quality control of diary products using single frequency admittance measurements*, Meas. Sci. Technol. 17 (2006) 275-280.

[17] M. Hanningsson, K. Östergren, and P. Dejmek, *The electrical conductivity of milk - The effect of dilution and temperature*, Int. J. Food Prop. 8 (2005) 15-22.

[18] B.A. Lawton, and R. Pethig, *Determining the fat content of milk and cream using AC conductivity measurements*, Meas. Sci. Technol. 4 (1993) 38-41.

[19] A. Sadat, P. Mustajab, and I.A. Khan, *Determining the adulteration of natural milk with synthetic milk using ac conductance measurements*, J. Food Eng. 77 (2006) 472-477.

[20] G. Mucchetti, M. Gatti, and E. Neviani *Electrical conductivity changes in milk caused by acidification: determining factors*, J. Dairy Sci. 77 (1994) 940-944.

[21] ABTECH Scientific, Inc. (Advanced Biochip Technologies), 800 East Leigh Street, Richmond, Virginia 23219, http://www.abtechsci.com/imes.html (last access on January, 13 2012).

[22] ABTECH Scientific, Inc. (Advanced Biochip Technologies), *IME Brochure*, http://www.abtechsci.com/pdfs/imebro02.pdf (last access on January, 13 2012).

[23] W. Olthuis, W. Streekstra, and P. Bergveld, *Theoretical and experimental determination of cell constants of planar-interdigitated electrolyte conductivity sensors*, Sens. Actuators, B 24-25 (1995) 252-256.

[24] S.S. Gevorgian, T. Martinsson, P.L.J. Linner, and E.L. Kollberg, *CAD Models for Multilayered Substrate Interdigital Capacitors*, IEEE Trans. Microw. Theory Tech. Vol. 44 No. 6 (1996) 896-904.

[25] R. Igreja, and C.J. Dias, *Analytical evaluation of the interdigital electrodes capacitance for a multi-layered structure*, Sens. Actuators, A 112 (2004) 291–301.

[26] M.W. Otter, *Approximate expressions for the capacitance and electrostatic potential of interdigitated electrodes*, Sens. Actuators, A 96 (2001) 140-144.

[27] M.C. Zaretsky, L. Mouyad, and J.R. Melcher, *Continuum properties from interdigitated electrode dielectrometry*, IEEE Trans. Electr. Insul. 23 (1988) 897-917.

[28] V.F. Lvovich, C.C. Liu., and M.F. Smiechowski, *Optimization and fabrication of planar interdigitated impedance sensors for highly resistive non-aqueous industrial fluids*, Sens. Actuators, B 119 (2006) 490-496.

[29] *Agilent Technologies Impedance Measurement Handbook*, Agilent Technologies (July 2006).

[30] *HP 4284A Precision LCR Meter*, Hewlett Packard (1988).

[31] *1260 Impedance/Gain-Phase Analyzer*, Solartron analytical (1996).

[32] LEVM fitting program by Dr. J. Ross Macdonald, http://www.jrossmacdonald.com/ (last access on January, 13 2012).

[33] *Standard solutions reproducing the conductivity of electrolytes*, International Organization of Legal Metrology, International Recommendation 56 (1981).

[34] Milk Composition - Species Table, http://classes.ansci.illinois.edu/ansc438/milkcompsynth/milkcomp_table.html (last access January, 13 2012).

[35] M. Becchi, L. Callegaro, F. Durbiano, V. D'Elia, and A. Strigazzi, *Novel impedance cell for low conductive liquids: Determination of bulk and interface contributions*, Rev. Sci. Instrum. Vol. 78 No. 11 (2007) 113902.

[36] P. Hauptmann, N. Hoppe, and A. Puettmer, *Ultrasonic Sensors for Process Industry*, IEEE Ultrasonic symposium Vol.1 (2001) 369-378.

[37] S. Rajagopalan, S. J. Sharma, and P. K. Dubey, *Measurement of ultrasonic velocity with improved accuracy in pulse echo setup*, Rev. Sci. Instrum. Vol. 7 (2007) 085104.

[38] D. Marioli, C. Narduzzi, C. Offelli, D. Petri, E. Sardini, and A. Taroni, *Digital Time-of-Flight Measurement for Ultrasonic Sensors*, IEEE T. Instrum. Meas., 41 (1992) 93-97.

[39] R. Raya, A. Frizera, R. Ceres, L. Calderón, and E. Rocon, *Design and evaluation of a fast model-based algorithm for ultrasonic range measurements*, Sens. Actuators, A 148 (2008) 335-341.

[40] *Underwater Acoustics, Technical Guides - Speed of Sound in Pure Water*, National Physical Laboratory, http://www.npl.co.uk/ .

[41] V. A. Del Grosso and C. W. Mader, *Speed of Sound in Pure Water*, J. Acoust. Soc. Am. Volume 52, Issue 5B, (1972) 1442-1446.

[42] F. Mantovani and C. Tagliaferri, *Signal conditioning of a hot-film anemometer for a periodic flow rate monitoring system*, Rev. Sci. Instrum. Vol. 82 No. 12 (2011) 126109.

[43] L. M. Fingerson", *Thermal anemometry, current state, and future directions*, Rev. Sci. Instrum. Vol. 65 No. 2 (1994) 285-300.

[44] H. H. Bruun, *Hot-Wire Anemometry: Principles and Signal Analysis*, Oxford University Press (1995).

[45] P. Ligęza, *Constant-bandwidth constant-temperature hot-wire anemometer*, Rev. Sci. Instrum. Vol. 78 No. 7 (2007) 075104.

[46] P. Ligęza, *Construction and experimental testing of the constant-bandwidth constant-temperature anemometer*, Rev. Sci. Instrum. Vol. 79 No. 9 (2008) 096105.

[47] K. Bremhorst and L. J. W. Graham, *A fully compensated hot/cold wire anemometer system for unsteady flow velocity and temperature measurements*, Meas. Sci. Technol. Vol. 1 No. 5 (1990) 425-430.

[48] G. R. Sarma and G. Comte-Bellot and T. M. Faure, *Software corrected hot wire thermal lag for the constant voltage anemometer featuring a constant bandwidth at the selected compensation setting*, Rev. Sci. Instrum. Vol. 69 No. 9 (1998) 3223-3231.

[49] M. Nabavi and K. Siddiqui, *A critical review on advanced velocity measurement techniques in pulsating flows*, Meas. Sci. Technol. Vol. 21 No. 4 (2010) 042002.

[50] A. Berson and P. Blanc-Benon and G. Comte-Bellot, *On the use of hot-wire anemometry in pulsating flows. A comment on ´A critical review on advanced velocity measurement techniques in pulsating flows'*, Meas. Sci. Technol. Vol. 21 No. 12 (2010) 128001.

[51] A. Berson and P. Blanc-Benon and G. Comte-Bellot, *A strategy to eliminate all nonlinear effects in constant-voltage hot-wire anemometry*, Rev. Sci. Instrum. Vol. 80 No. 4 (2009) 045102.

[52] S. Takagi, *A hot-wire anemometer compensated for ambient temperature variations*, J. Phys. E: Sci. Instrum. Vol. 19 No. 9 (1986) 739-743.

Acknowledgements

I thought several times about the language to use in the acknowledgements. I chose the one with which I could better express my feelings, for being sure that the people which this message is addressed to, will receive it. Sorry English, I cannot handle you well yet. My tutor can confirm it.

Senza alcun dubbio, la persona che ha reso possibile il mio lavoro di ricerca è il mio Tutor, il Prof. Giovanni Chiorboli, che con una grande correttezza e generosità mi ha sempre supportato in questi anni. Mi ha sempre seguito con costanza e attenzione coinvolgendomi anche in stimolanti attività che potessero arricchire le mie conoscenze. Un *grazie* a parte gli è inoltre dovuto per l'infinita pazienza che ha avuto nella revisione della mia tesi, perfino io avrei avuto gli incubi al solo pensiero.

Un altro *grazie* va ai miei genitori che non hanno mai dubitato di me lasciandomi sempre la più completa libertà di scelta, ammetto che senza il loro supporto mi sarei trovato in seria difficoltà in alcune situazioni.

Come non citare a questo punto la mia *compagnia del treno*, con cui ho condiviso le mie 3 quotidiane ore di viaggio, e tutti i ragazzi della palazzina 4 che mi hanno sempre aspettato seduti in mensa... ma sono davvero così lento a mangiare?

Una doverosa nota d'onore va anche al mitico tecnico della palazzina, non ricordo nemmeno il numero di volte in cui ho avuto bisogno di lui per risolvere i problemi più disparati, *grazie* Sisko! Il mio MacGyver di fiducia, ma anche una gran persona.

Infine, un *grazie* va anche a tutti gli ormai ex-studenti, che spero di poter considerare amici, che durante questi anni hanno collaborato con me durante la loro tesi e che hanno in qualche modo contribuito al mio lavoro.